

**This document is a preprint submitted to EarthArXiv**

Soil moisture effects on InSAR - a correction approach and example from a hyper-arid region

Authors: RBLohman and PM Bürgi

Highlights:

InSAR phase changes due to soil moisture are repeatable during different rain events

Exponential distribution of soil moisture sensitivity predicts observed phase effects

Model based on previous events improves InSAR quality for subsequent events

## Abstract

We present Interferometric Synthetic Aperture data spanning a series of precipitation events that impacted the southern edge of the Arabian Peninsula in 2017-2018. The arid climate, sparse vegetation and low topographic relief result in very high interferometric coherence between most pairs of dates, even for those separated by multiple years. For pairs of dates with differing soil moisture conditions, such as a “dry” date and a date immediately following one of the precipitation events, the interferometric coherence magnitude is much lower. However, pairs spanning the same event, but with a longer time interval, often have high interferometric coherence magnitude. This observation suggests that the phase changes that result in lower coherence for some pairs are not permanent, such as those that would result from erosion or deposition of material, but are due to the variations in soil moisture. In support of this view, when we compare the phase of individual pixels to their neighbors, we observe similar phase change trends for each precipitation event. We present a simple statistical model of the relationship between soil moisture and phase, and show that it predicts the observed coherence and phase histories within this particular SAR time series. We also show how the parameters of this relationship can be inferred from the InSAR observables, and can be used to reduce the soil moisture effects on coherence and phase even for pairs of dates that were not used in that parameter estimation. We present results for synthetic time series, including a demonstration of the widely-observed phenomenon that displacement rates inferred from InSAR time series depend on the choice of interferometric pairs used in the analysis.

## 1.0 Introduction

Interferometric synthetic aperture radar (InSAR) observations have applications in a wide range of research areas involving ground displacements, and are increasingly used in studies of hydrologic systems where the observed signals are associated with seasonality, human interventions and droughts (e.g., Bell et al., 2008; Chaussard et al., 2017; Murray and Lohman, 2018; Wetzler et al., 2019; Neely et al., 2021; Cigna and Tapete, 2021; Murray et al., 2021). Variations in soil and vegetation water content also impact the scattering and emission at microwave wavelengths, and synthetic aperture radar (SAR) and passive microwave observations are used to constrain soil moisture in a range of environments (e.g., Dubois et al., 1995; Ulaby et al., 1996; Bartalis et al., 2007; Barrett et al., 2009; Das et al., 2010; Entekhabi et al., 2010; Jackson et al., 2010; Draper et al., 2012; Mladenova et al., 2014; Colliander et al.,

2017). Effects of soil moisture changes on interferometric phase have also been observed since InSAR data first became widely available (e.g., Gabriel et al., 1989; Nolan et al., 2003; Nolan and Fatland, 2003; Rabus et al., 2010), prompting concerns about how soil moisture may impact estimates of ground deformation. These concerns have only become more relevant as the quality of SAR imagery catalogs improves, particularly in areas with a mix of agricultural activity, tectonics, and other potential signal sources (e.g., Jiang and Lohman, 2021), where it may be difficult to separate the effects of ground displacement from those of soil moisture (e.g., Zwieback et al., 2017) .

Here we focus on a hyperarid region along the southern edge of the Arabian Peninsula (Figure 1). This region is characterized by sparse vegetation and intense but infrequent precipitation events, allowing us to separate the impact of soil moisture on InSAR time series from the other factors that dominate the signals elsewhere. We show how the examination of full-resolution, high-pass filtered interferograms allows us to characterize the pixel-to-pixel variability of the soil moisture response. We present a coherence-based correction approach, examples using synthetic data, and demonstrate how we can use data from as few as two events to model the expected soil moisture effects and apply the correction to a completely independent interferogram spanning a separate precipitation event not used in the modeling.

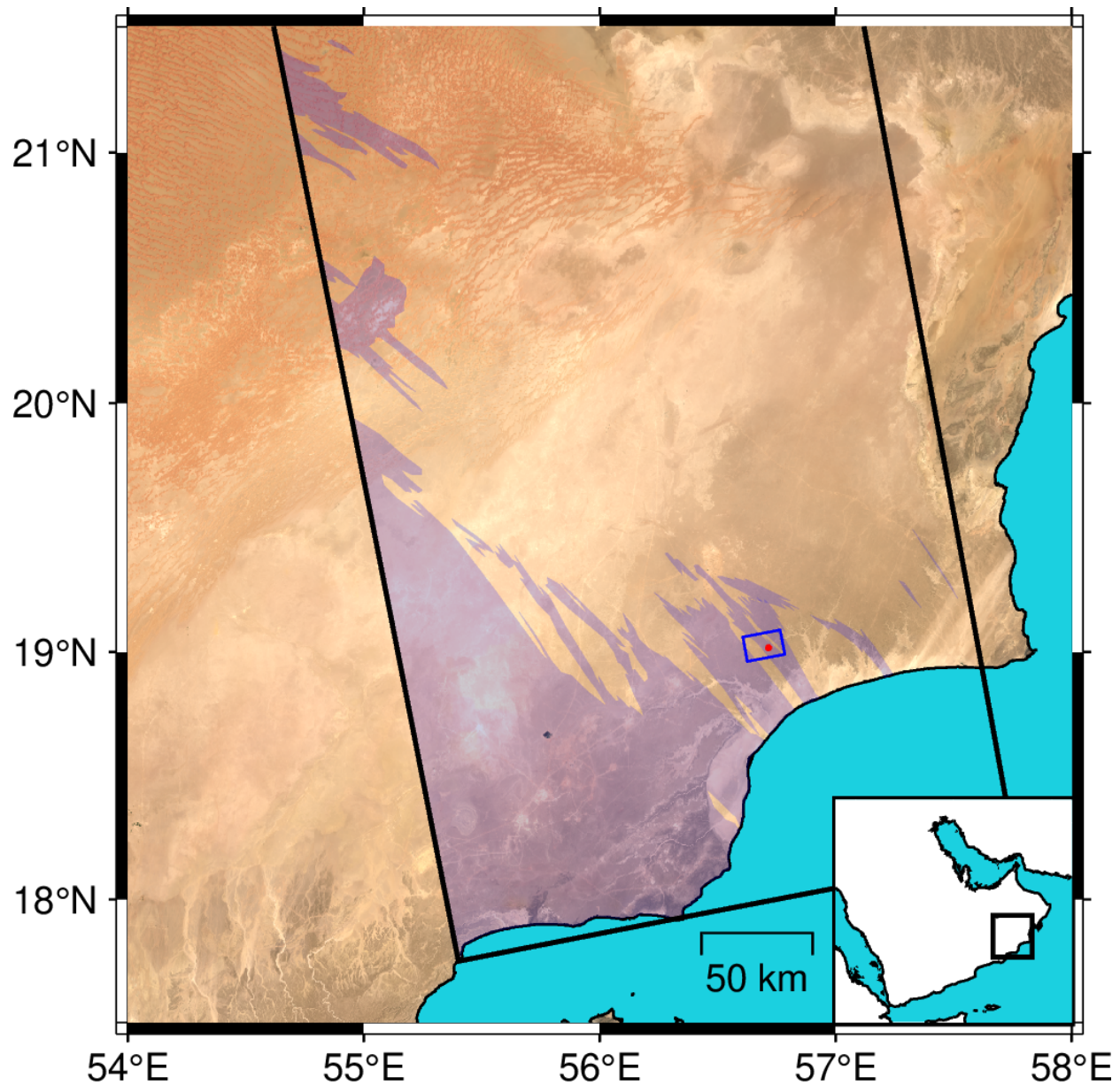


Figure 1: Study region along southern edge of Arabian Peninsula (map area shown in inset) with location of Sentinel-1 Track 130 (black outline), and Landsat-8 imagery (color). Reddish regions in the northwest are sand dune fields. Light blue overlay indicates the approximate region impacted by Typhoon Mekunu (Figure 2). Red circle indicates pixel shown in Figures 3 and 4, at latitude 19.0172, longitude 56.7145, red box shows region of full-resolution data shown in Figure 11.

## 2.0 Data

We use C-band observations from the European Space Agency's Sentinel-1a satellite (e.g., Torres et al., 2012) for track T130 on 63 dates between February 12, 2017 and January 21, 2019. During this time period imagery was acquired during every 12-day repeat. No observations were acquired by the Sentinel-1b satellite, so there are no 6-day repeats available

at this location during this time period. We process the SAR imagery with the InSAR Scientific Computing Environment (ISCE) package (Rosen et al., 2012), using the stack processor add-on (Fattahi et al., 2017) to generate a stack of coregistered, full-resolution single-look complex (SLC) images with the effects of topography removed using the Shuttle Radar Topography Mission (SRTM) digital elevation model (Farr et al., 2007).

Here we define the basic quantities that we derive from the SAR imagery, following the standard nomenclature used in the discipline where possible (e.g., Ulaby, 1981; Zebker and Villasenor, 1992; Rosen et al., 2000; Hanssen, 2001; Woodhouse, 2017). For each SAR image  $u_j(t_k)$  is the complex-valued observation associated with pixel  $j$  at time  $t_k$ , with amplitude  $|u_j(t_k)|$  and phase  $\arg(u_j(t_k))$ . The full-resolution, complex-valued interferogram,  $\psi_j(t_a, t_b)$ , between any two dates,  $t_a$  and  $t_b$ , at a given point,  $j$ , is:

$$\psi_j(t_a, t_b) = u_j(t_a)u_j(t_b)^* \quad \text{Eq. 1}$$

where  $u_j(t_b)^*$  indicates the complex conjugate. The phase of the full-resolution interferogram is  $\phi_j(t_a, t_b) = \arg(\psi_j(t_a, t_b))$ . The values of  $\phi_j(t_a, t_b)$  are “wrapped”, meaning that they are restricted to the interval  $-\pi$  to  $\pi$ , even though the “true” signal (deformation, atmospheric, etc.) that produces these phase delays can span a much wider range. The phase values associated with these “true” signals,  $\phi_j^{true}(t_a, t_b)$ , are often referred to as the “unwrapped” phase values, and differ from the “wrapped” values by integer factors of  $2\pi$  for the full-resolution data (e.g., Chen and Zebker, 2002). For noisier data, or regions with a high strain rate, the number of  $2\pi$  cycles between points can be ambiguous.

We examine a measure of the spatial variability of each interferogram, generally referred to as the “complex coherence”,  $\gamma$ .

$$\gamma_j(t_a, t_b) = \frac{E[\psi_j(t_a, t_b)]}{\sqrt{E[|u_j(t_a)|^2]} \sqrt{E[|u_j(t_b)|^2]}} \quad \text{Eq. 2}$$

where  $E[x]$  indicates the expectation of a variable,  $x$ . For real-world data, the expectations are generally estimated as the mean over some number,  $N$ , of points in the vicinity of pixel  $j$ :

$$\hat{\gamma}_j(t_a, t_b) = \frac{\sum_{l=1}^N \psi_l(t_a, t_b)}{\sqrt{\sum_{l=1}^N |u_l(t_a)|^2} \sqrt{\sum_{l=1}^N |u_l(t_b)|^2}} \quad \text{Eq. 3}$$

The magnitude of the complex coherence,  $|\hat{\gamma}_j(t_a, t_b)|$  is often simply referred to as the “coherence”, or “coherence magnitude” in the literature (e.g., Zebker and Villasenor, 1992) and is a measure of the spatial heterogeneity of the phase in a given interferogram. Coherence

values near unity indicate that the phase varies smoothly in space, whereas coherence will be below  $\sim 0.3$  in regions where the phase is dominated by noise.

We use  $\overline{\Phi}_j^{wrap}(t_a, t_b) = \arg(\widehat{\gamma}_j(t_a, t_b))$  to refer to the phase of the complex coherence, which is also the phase of the spatially averaged, complex-valued interferogram. The averaging operation applied to the complex-valued phase vectors in Equation 3 is a nonlinear function of the phase of the  $N$  pixels included in that average. In general the average of the real-valued “unwrapped”, or “true” phase values over those same pixels will not be exactly the same as the phase of the averaged complex values, with the differences increasing as the noise level or

strain within the averaging window increases. We use  $\overline{\Phi}_j^{true}(t_a, t_b) = \frac{1}{N} \sum_{l=1}^N \Phi_j^{true}(t_a, t_b)$  to

indicate the average of the unwrapped phase values. For real-world data, it may be challenging or impossible to unwrap full-resolution, unfiltered data, but for synthetic scenarios the unwrapped phase values can be fixed by the researcher. In Section 3 we use synthetic data to show the differences between these phase averages and how they vary with the type of signal, surface properties and processing approach.

As discussed in Bürgi and Lohman, 2021, the interferometric coherence (i.e., coherence magnitude) in this region is generally quite high ( $|\gamma| > 0.9$ , Figure 2), even for interferograms spanning more than a year. The exceptions are in regions with sand dunes and areas of high topographic relief along the coast and along gullies. Interferograms between pairs where one image is taken on a dry date and one image is taken immediately after a precipitation event are associated with very low coherence, even when the pair only spans a short time interval (Figure 2b). The coherence magnitudes shown in Figure 2 all share the same first date (2018-05-02), and span 12, 24, and 36 days, respectively. The second image of the pair shown in Figure 2b was acquired right after a very large storm, Typhoon Mekunu, passed over the region. Dark regions in Figure 2b indicate areas of lower coherence, including bands stretching outwards to the north of the main area impacted by the typhoon. However, the same “dry” image paired with an image taken on another dry date after the storm (Figure 2c), is nearly as coherent as the 12-day pair before the event (Figure 2a). Both of the interferograms shown in Figures 2b and 2c span the time interval of the storm - the high coherence of the longer-time-interval pair indicates that the lower coherence we see in Figure 2b is due to a temporary change in scattering properties, presumably associated with the change in soil moisture associated with the typhoon, rather than to any permanent changes to the surface (e.g., erosion, deposition).

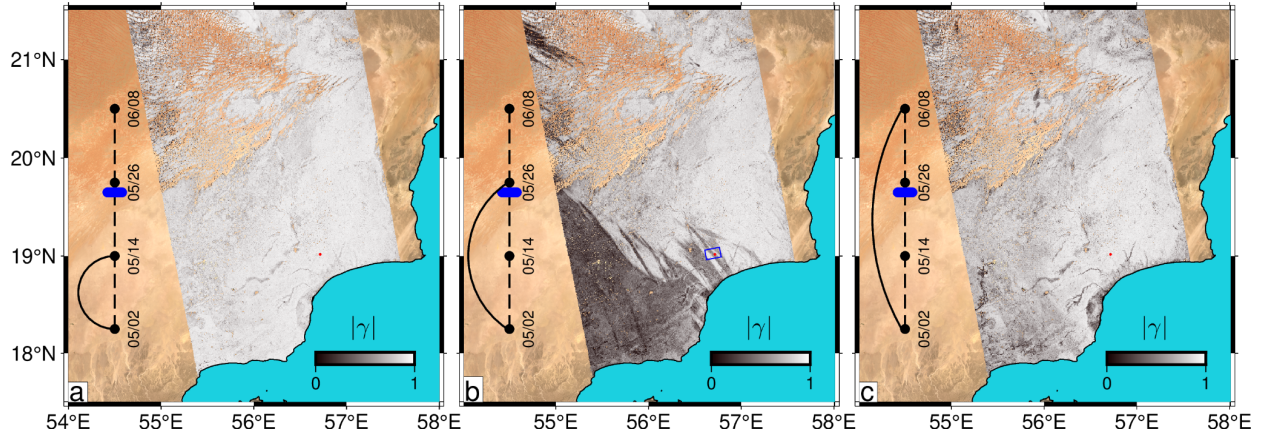


Figure 2: Coherence magnitude,  $|\gamma|$ , in grayscale for three VV interferograms that all share the same first date, 2018-05-02, with second dates 2018-05-14 (a), 2018-05-26, immediately after Typhoon Mekunu (b), and 2018-06-08 (c). Timespan also shown in diagram on left, with blue bar indicating timing of Typhoon Mekunu. Note that even though the interferogram in (c) has a longer time interval than the interferogram in (b), it is associated with higher coherence. Regions in the northwest that are covered by sand dunes are always associated with lower coherence and are masked out. Red dot and blue box as in Figure 1.

We can examine this effect further by looking at the coherence magnitude for all possible pairs of dates within the time series (Figure 3a), at a location that was impacted by at least three events between late 2017 and 2018 (red circle in Figure 1). Note that coherence over even two full years is quite high compared to the coherence of the shortest-time-interval pairs associated with the rain events. Also note that coherence between “wet” dates (where the blue/green lines intersect) is relatively high, indicating that the scattering behavior of the surface is similar during each wetting event. We also look at the high-pass filtered phase (Figure 3b), which here is the phase of the complex conjugate between the unfiltered, full-res interferograms and the complex coherence (Equation 3). By removing longer-spatial-scale signals from each pair, we can focus on how the pixel-to-pixel variability changes over time. Note that in time periods affected by rain, when there is a decrease in coherence magnitude, the phase of the pixel shown in Figure 3b shifts relative to its neighbors in a consistent manner. In Figure 3c we show the coherence magnitude vs. high-pass filtered phase, colored by the difference in backscatter amplitude between each pair of dates. The difference in amplitude also changes in a consistent manner as the phase change increases and coherence magnitude decreases.

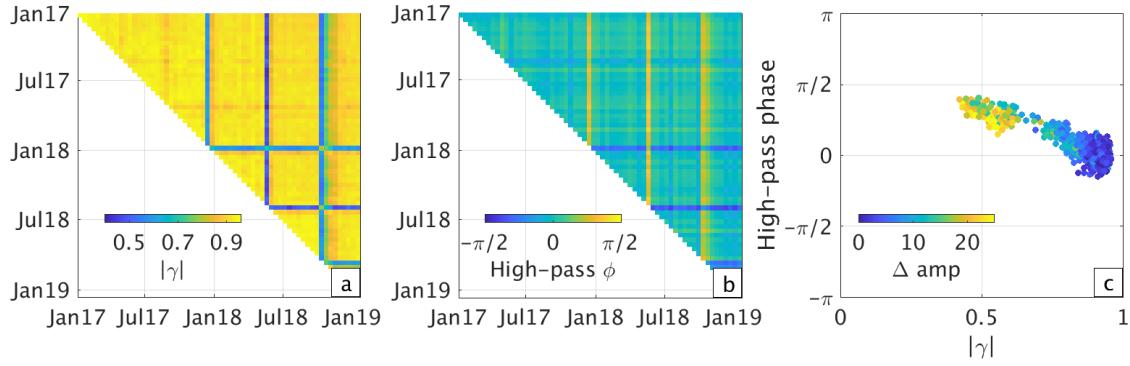


Figure 3: Observed phase characteristics in vicinity of pixel at location in Figure 1. a) Coherence magnitude for all possible pairs of dates. Top row indicates all pairs with respect to the first date, and the diagonal is for the shortest timespan interferograms between adjacent dates. b) High-pass filtered phase, using a Gaussian window with width and length 10 pixels around the same point. c) Coherence magnitude from (a) vs. high-pass filtered phase from (b). For clarity, the high-pass filtered phase has been multiplied by  $-1$  or  $+1$ , depending on whether the inferred soil moisture change for that pair (see below) is positive or negative.

We also examine the quantity known as phase closure (e.g., De Zan et al., 2014, 2015; Gruber et al., 2016; De Zan and Gomba, 2018; Michaelides and Zebker, 2019; Molan and Lu, 2020; Benoit et al., 2020; Molan et al., 2020; Maghsoudi et al., 2022; Zheng et al., 2022). Phase closure analysis involves the comparison of the spatially downsampled or filtered phase between different combinations of interferometric pairs that span the same time interval. The nonlinearity involved in averaging of complex-valued vectors means that spatial averaging or filtering will result in differences between such combinations, to a degree that increases with the noise level or complexity of phase within the averaging window. Phase closure has been used in efforts to understand soil and vegetation water content variability (e.g., De Zan et al., 2014; Gruber et al., 2016; De Zan and Gomba, 2018; Molan and Lu, 2020; Michaelides and Zebker, 2019) as well as in efforts to avoid attributing effects due to soil moisture as deformation (e.g., Zwieback et al., 2017; Benoit et al., 2020; Maghsoudi et al., 2022; Zheng et al., 2022) The “triplet” between three dates can be defined as

$$\tau_{a,b,c} = \arg \left[ \hat{\gamma}_j(t_c, t_a)^* \hat{\gamma}_j(t_c, t_b) \hat{\gamma}_j(t_b, t_a) \right] \quad \text{Eq. 4}$$

As in Maghsoudi et al., 2022, we also examine phase closure for combinations of more than three dates. We consider the set of all pairs with a given timespan (e.g., 12-days, 24-days, etc.) that are within the time interval between two dates,  $t_a$  and  $t_b$ :

$$T_n(t_a, t_b) = \arg \left[ \hat{\gamma}_j(t_b, t_a)^* \prod_{k=1}^{(t_b-t_a)/n} \hat{\gamma}_j(t_a + kn, t_a + (k-1)n) \right] \quad \text{Eq. 5}$$

where the  $\hat{\gamma}_j(t_b, t_a)^*$  term is the complex conjugate of the longest time-span, spatially averaged/filtered interferogram, and the product that immediately follows includes all intervening pairs with timespan  $n$ . For instance,  $T_{12}(t_1, t_a)$  is the phase closure between the interferogram between the first date and  $t_a$ , and all of the shortest (12-day) pairs between  $t_1$  and  $t_a$ . Note that when there is no filtering or spatial averaging, phase closure is zero by definition.

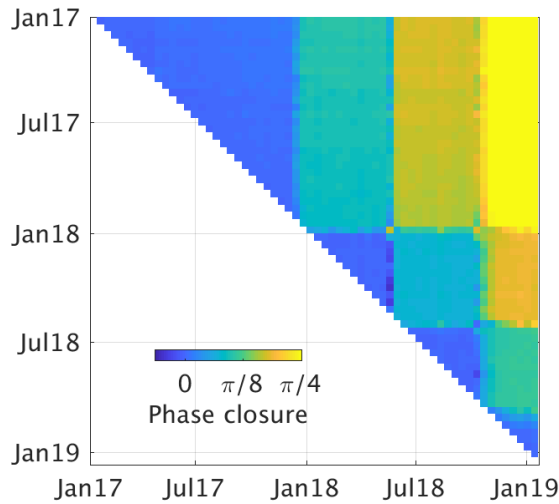


Figure 4. Phase closure for all possible  $T_{12}(t_a, t_b)$  for the 63 dates in the Sentinel-1 timeseries. The upper right corner in this diagram corresponds to the longest possible interferogram compared with the product of all 12-day pairs in between the first and last date. Each “step” in phase closure is associated with a time period with a precipitation event when we also observe a temporary drop in coherence.

In Figure 4, it is apparent that phase closure in this region is negligible during most time periods (i.e., the value of  $T_{12}(t_a, t_b)$  does not change as the timespan of the interferogram between  $t_a$  and  $t_b$  increases), but has a clear, non-zero bias during the three time periods that precipitation events. In Section 3, we examine some synthetic models that reproduce this observation as well as the high-pass filtered phase and coherence observations, and demonstrate the effectiveness of a correction for the soil-moisture-based contribution to the phase based on this model

## 3.0 Methods

### 3.1 Spatial averaging and phase closure

Below, we explore several synthetic scenarios in order to demonstrate that the observations we have made using real data can be reasonably explained using a fairly simple relationship between soil moisture and the phase perturbation at each pixel. The actual relationships are

certainly more complex than those we explore here, but the synthetic examples allow us to take the additional step of exploring how some commonly used filtering/spatial averaging operations (e.g., “taking looks”) affect scenarios even where no deformation is present, and to provide some idea of the biases that can result from filtering/spatial averaging alone. In Appendix A.1 we show a simple case of averaging of three pixels and illustrate how the coherence magnitude and closure phase are affected by the distribution of phase amongst those three pixels, and in Appendix A.2 we show the extension to averages over a large number of pixels and three dates.

In the model explored here, each pixel is associated with a time-invariant “soil moisture sensitivity”,  $s_j$ , with no spatial correlation between pixels. The key factor that impacts the behavior of a spatial average of these pixels is the statistics of  $s$  - if the distribution of  $s$  is asymmetric (such as an exponential distribution), we will show that we expect phase closure biases similar to those we see in the real-world observations, while a symmetric distribution of  $s$  will result in non-zero phase closure but no bias (i.e., the expectation is zero). We also define  $m_k$ , a dimensionless, positive value associated with a measure of soil moisture on each date,  $t_k$ .  $m_k$  is zero when the soil is completely dry, and increases with soil moisture.

If we assume that the phase change associated with soil moisture is linearly related to  $m_k$  through the soil moisture sensitivity,  $s$ , then for an interferogram between two dates where only the soil moisture changes, we have:

$$\psi_j(t_b, t_a) = e^{-i(m_b - m_a)s_j} = e^{i\Delta m_{ab}s_j} \quad \text{Eq. 6}$$

where  $\Delta m_{ab} = m_a - m_b$ . Note that for the remainder of this paper we generally use the convention where the complex conjugate is taken on the earlier date,  $\psi_j(t_b, t_a) = u_j(t_b)u_j(t_a)^*$ , with  $t_b$  occurring after  $t_a$ . In this model, if date  $t_a$  is “dry” and  $t_b$  is “wet”, we would see a negative phase change, or an apparent uplift. The “soil moisture” phase at a given pixel,  $\phi_j^{sm}$ , is  $\Delta m_{ab}s_j$ , wrapped on the  $2\pi$  interval. We begin by examining the expected result if  $s$  is distributed according to the exponential distribution, which is highly asymmetric. We compare these results against several other distributions (including a normal distribution) in Table 1.

If  $s$  is a random variable that follows the exponential distribution (a type of Gamma distribution,  $\Gamma(1, 1)$ , with shape parameter = 1 and scale parameter = 1), its probability density function,  $f_s(s)$ , has the following form:

$$f_{s,exp}(s) = e^{-s} \text{ for } s \geq 0, 0 \text{ for } s < 0 \quad \text{Eq. 7}$$

We can use the properties of this distribution to evaluate the effect of spatial averaging of an interferogram over  $N$  pixels on the coherence and phase of that average. Because the soil moisture-related perturbations to the phase is wrapped along the interval between  $-\pi$  and  $\pi$ , the averaging operation is nonlinear and is not the same as for real-valued data. To evaluate the average of the complex-valued phase, we examine the real and imaginary portions separately, and calculate the expected value for each. The spatially averaged interferogram between images acquired on dates  $t_a$  and  $t_b$  for a case where the only contribution to the interferogram comes from the soil moisture term is:

$$\overline{\Psi}_j(t_b, t_a) = \frac{1}{N} \sum_{j=1}^N \Psi_j(t_b, t_a) = \frac{1}{N} \sum_{j=1}^N e^{i\Delta m_{ab} s_j} = \widehat{\gamma}_j(t_b, t_a) \approx E[e^{i\Delta m_{ab} s}] = E[\cos(\Delta m_{ab} s)] + i E[\sin(\Delta m_{ab} s)] \quad \text{Eq. 8}$$

For the first term (real component), we use the definition of the expected value of a function of a random variable:

$$E[\cos(\Delta m_{ab} s)] = \int_0^{\infty} \cos(\Delta m_{ab} s) f_{s,exp}(s) ds = \frac{1}{\Delta m_{ab}^2 + 1} \quad \text{Eq. 9}$$

Similarly, for the imaginary component:

$$E[\sin(\Delta m_{ab} s)] = \int_0^{\infty} \sin(\Delta m_{ab} s) f_{s,exp}(s) ds = \frac{\Delta m_{ab}}{\Delta m_{ab}^2 + 1} \quad \text{Eq. 10}$$

so that the expected value of the spatially averaged interferogram (complex coherence) in the vicinity of the  $j^{\text{th}}$  pixel is:

$$\widehat{\gamma}_j(t_b, t_a) \approx \frac{1}{\Delta m_{ab}^2 + 1} + i \frac{\Delta m_{ab}}{\Delta m_{ab}^2 + 1} \quad \text{Eq. 11}$$

The expected value of the coherence magnitude for a given pair is:

$$|\widehat{\gamma}_j(t_b, t_a)| \approx \sqrt{\left(\frac{\Delta m_{ab}}{\Delta m_{ab}^2 + 1}\right)^2 + \left(\frac{1}{\Delta m_{ab}^2 + 1}\right)^2} = \sqrt{\frac{\Delta m_{ab}^2 + 1}{(\Delta m_{ab}^2 + 1)^2}} = \sqrt{\frac{1}{\Delta m_{ab}^2 + 1}} \quad \text{Eq. 12}$$

Similarly, for any value of  $|\widehat{\gamma}_j(t_b, t_a)|$ , the corresponding  $\Delta m_{ab}$  is:

$$\Delta m_{ab}(|\widehat{\gamma}_j(t_b, t_a)|) \approx \sqrt{\frac{1}{|\widehat{\gamma}_j(t_b, t_a)|^2} - 1} \quad \text{Eq. 13}$$

The expected phase of an average of complex-valued pixels for a given  $\Delta m_{ab}$ , is:

$$\arg[\hat{\gamma}_j(t_b, t_a)] \approx \tan^{-1}\left(\frac{im}{re}\right) = \tan^{-1}\left(\frac{\frac{\frac{\Delta m_{ab}}{\Delta m_{ab}^2 + 1}}{\frac{1}{\Delta m_{ab}^2 + 1}}}{\frac{\Delta m_{ab}}{\Delta m_{ab}^2 + 1}}}\right) = \tan^{-1}(\Delta m_{ab}) \quad \text{Eq. 14}$$

Distribution	$f_s(s)$	$E[\cos(\Delta ms)]$	$E[\sin(\Delta ms)]$	$E[\hat{\gamma}]$	$E[\arg[\hat{\gamma}]]$	$E[\Delta ms]$
Normal ( $\mu = 1$ )	$\frac{1}{\sigma\sqrt{2\pi}}e^{-\frac{1}{2}\left(\frac{s-1}{\sigma}\right)^2}$	$e^{-\frac{\sigma^2\Delta m^2}{2}}\cos(\Delta m)$	$e^{-\frac{\sigma^2\Delta m^2}{2}}\sin(\Delta m)$	$e^{-\frac{\sigma^2\Delta m^2}{2}}$	$\Delta m$	$\Delta m$
$\Gamma(1, 1)$ (exponential)	$e^{-s}$	$\frac{1}{1+\Delta m^2}$	$\frac{\Delta m}{1+\Delta m^2}$	$\frac{1}{(1+\Delta m^2)^{1/2}}$	$\tan^{-1}(\Delta m)$	$\Delta m$
$\Gamma(2, 1/2)$	$4se^{-2s}$	$\frac{1-\frac{\Delta m^2}{4}}{\left(1+\frac{\Delta m^2}{4}\right)^2}$	$\frac{\Delta m}{\left(1+\frac{\Delta m^2}{4}\right)^2}$	$\frac{1}{1+\frac{\Delta m^2}{4}}$	$\tan^{-1}\left(\frac{\Delta m}{1-\frac{\Delta m^2}{4}}\right)$	$\Delta m$

Table 1: Expected behavior of three distributions with probability distribution  $f_s(s)$  for a given change in soil moisture metric between two dates,  $t_a$  and  $t_b$ ,  $\Delta m_{ab}$ . Here, we use  $\Delta m_{ab} = \Delta m$  and  $\hat{\gamma}_j(t_b, t_a) = \hat{\gamma}$  for brevity. Expectation of the real and imaginary parts of a spatially averaged interferogram, the complex coherence magnitude and phase, and the expected value of the real-valued, “unwrapped” phase (right-most column),  $E[\Delta ms]$  are given for a normal distribution and two Gamma distributions, with parameters described in the leftmost column. Other parameters ( $\mu$ ,  $\theta$ ) are chosen so that each distribution has the same mean=unity and the real-valued average of  $E[\Delta ms] = \Delta m$ .

In Table 1 we compare the expected characteristics of the spatial averages of interferograms generated with normally-distributed  $s$ , with the exponential distribution,  $\Gamma(1, 1)$ , and for another variant of the Gamma distribution,  $\Gamma(2, 1/2)$ . Note that the expected value of the phase of the average of the complex-valued data,  $E[\arg[\hat{\gamma}]]$ , is the same as the average of the real-valued, unwrapped data,  $E[\Delta ms]$ , for the normal distribution, but differs for the two asymmetric distributions due to the  $\tan^{-1}$  terms. In Figure 5 we show the probability distributions for  $s$ , coherence magnitude and difference between the phase of the spatial average of the unwrapped (real-valued) and wrapped (complex-valued) data for these three distributions. In the next section we describe how the nonlinearities involved in these differences impact the phase, coherence magnitude and inferred deformation time series.

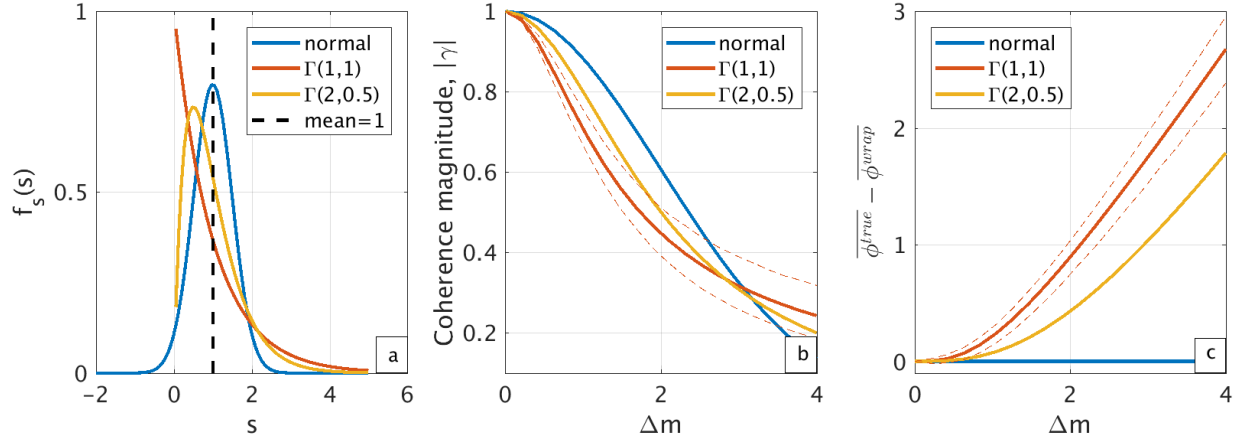


Figure 5: a) Probability distribution of pixel sensitivity,  $s$ , for a normal distribution (blue), exponential distribution (red) and gamma distribution with shape factor=2 and scale factor=1/2 (yellow). Parameters of each distribution (e.g., mean, rate, scale) are chosen such that they have the same mean value = 1 (black dashed line). b) Coherence magnitude  $|\hat{\gamma}|$  vs.  $m$  for each of the three distributions. c) Difference between “true” phase average (spatial average of unwrapped, real-valued phase,  $\overline{\phi^{true}}$ ) and the phase of the average of the wrapped data,  $\overline{\phi^{wrap}}$ . This is equivalent to the difference between the rightmost two columns in Table 1. Note that the difference is zero for the normal distribution. Red dashed lines in (b) and (c) indicate the  $1\sigma$  error bounds on coherence and phase bias when estimated over a sample of 100 pixels for the exponential distribution, for 10,000 trials.

### 3.2. Synthetic scenarios

To examine the effects of this soil moisture model on phase closure and inferred displacement for InSAR time series, we generate synthetic data with  $s$  drawn from the same exponential distribution described above, and impose a soil moisture history,  $m_k$ , with characteristics similar to what we observe in our real-world example. In Figure 6, we show results for a time series including three precipitation events, each followed by two dates with decreasing soil moisture. Coherence (Figure 6b) and phase closure (Figure 6c,d) for the synthetic data generated using the time series in Figure 6a vary in the same manner that we observe in the real data. While the model described in section 3.1 is likely a vast oversimplification of the real world, it can reproduce the features that we observe in the real InSAR timeseries at the times of the known precipitation events.

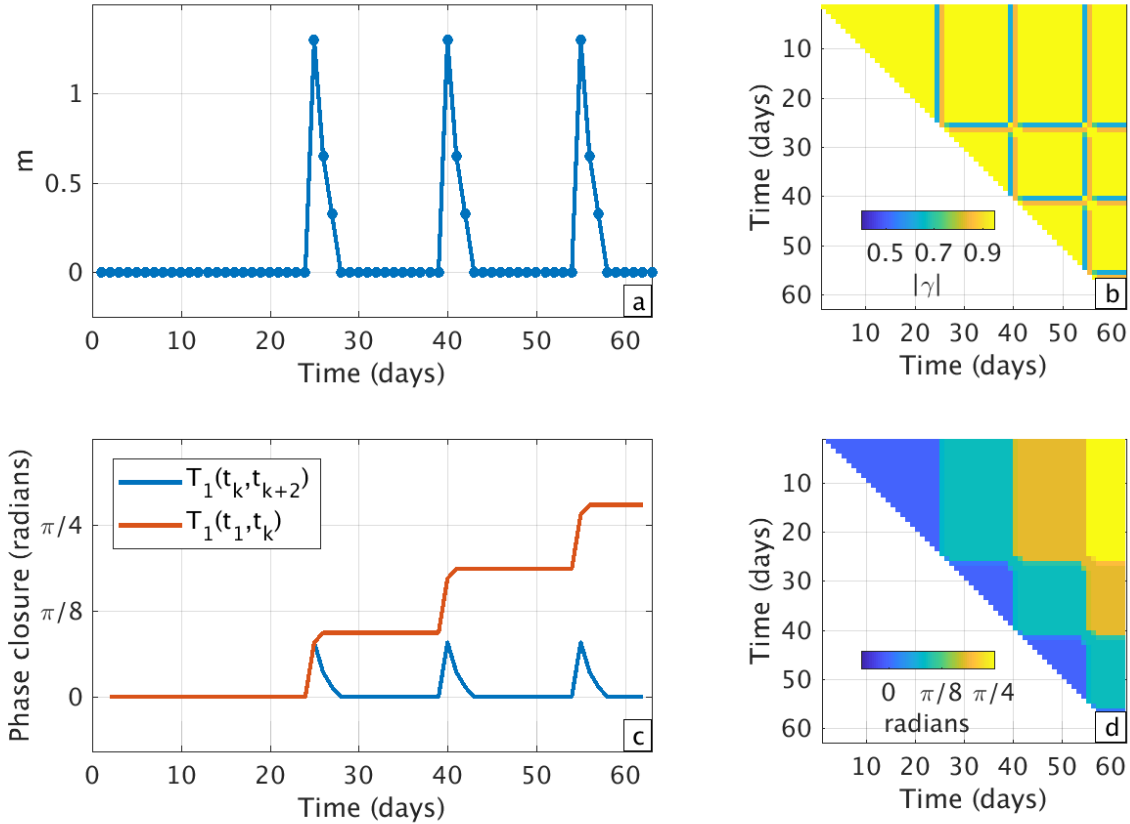


Figure 6: a) Time series of  $m_k$  with three pulses each followed by two dates during which soil moisture returns to the “dry” state. b) Coherence magnitude, for all possible pairs of dates, same colorscale as Figure 3a. c) Profiles of  $T_1(t_1, t_k)$  (red) and  $T_1(t_k, t_{k+2})$  (blue). d) Phase closure for all sets of  $T_1(t_a, t_b)$ . Top row are the  $T_1(t_1, t_k)$  for  $k = 3:n$  (red line in panel c), and values on the diagonal are the triplets between each possible set of three adjacent dates,  $T_1(t_k, t_{k+2})$ , blue line in panel c.

We can also quantify the effect on inferred deformation time series from various sets of interferograms spanning shorter or longer time intervals. In Figure 7, we show the interferograms between all pairs relative to the first date (Figure 7a) and for the shortest-timescale interferograms between sequential dates (Figure 7b) for the unwrapped (i.e., the “true” average,  $\Delta m_{ab}$ , black lines) and the wrapped spatial averages (red and blue lines). As shown in Table 1, the expected values of the spatially averaged wrapped interferograms are  $\tan^{-1}(\Delta m_{ab})$ , while the “true” values are  $\Delta m_{ab}$ . This difference is present even when the phase variability is much smaller than  $\pi$ , since it follows from the nonlinear averaging of the complex-valued vectors compared with the linear averaging of the real-valued, unwrapped, phase.

If we use these two sets of interferograms to infer the history of phase over time (Figure 7c), we get the “correct” history using either set of unwrapped interferograms, since there is no bias

introduced during the averaging process (black curve, Figure 7c). For the set of wrapped interferograms relative to the first date, the inferred time series (red line, Figure 7c) is still similar to the original, unwrapped time series (i.e., there is no long-term trend), but smaller due to the  $\tan^{-1}$  term. However, if we use only the shortest-timescale interferograms, which are often heavily relied on in InSAR time series analyses, the negative and positive  $\tan^{-1}$  terms associated with the soil moisture pulses do not cancel out, but result in a steady apparent increase over time. Inclusion of the second-shortest (24-day) interferograms as well as the shortest (magenta line, Figure 7c) results in a time series that is closer to the input signal (black curve), but still includes a bias that increases with each event.

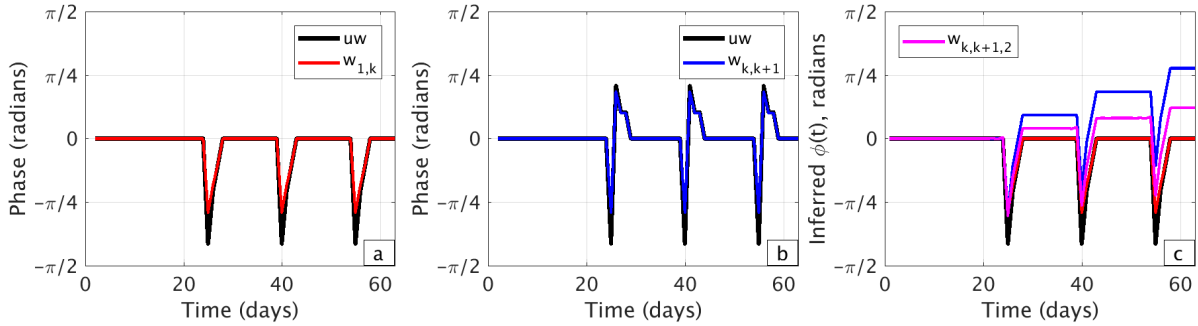


Figure 7: a) Time series of interferometric phase for all pairs beginning with the first date,  $\psi(t_k, t_1)$  vs. the date of the 2nd image, with both the true, or “unwrapped phase” (black,  $uw$ ) and wrapped phase (red,  $w_{1,k}$ ), averaged over 100 pixels. b) Same as (a), but for the phase of the shortest-timescale interferograms,  $\psi(t_{k+1}, t_k)$  vs. date of the 2nd image (average of unwrapped phase in black, average of wrapped phase,  $w_{k,k+2}$ , in blue). c) Time series of phase inferred from the unwrapped phase (black), and for the wrapped averaged phase for the cases in (a) and (b), as well as for the set of shortest- and next-shortest (skipping one date) interferograms,  $\psi(t_{k+1}, t_k)$  and  $\psi(t_{k+2}, t_k)$ , (magenta,  $w_{k,k+1,2}$ ).

The non-zero inferred average displacement rate that is induced here stems from the  $\tan^{-1}$  term in the phase of the average of the complex-valued interferogram (Table 1) and the fact that there are multiple dates impacted by each event (i.e., the “drying out” period). A scenario where the soil moisture signal only affected one date would result in no long-term bias - the bias follows from the asymmetry in how the wetting and drying periods are sampled, and the nonlinearity in the  $\tan^{-1}$  term.

### 3.3: Correction approach

For the synthetic scenarios where we add no other sources of noise and know the underlying statistical distribution of  $s$ , it is trivial to solve for  $s$  and remove the effects of soil moisture on each date.

Synthetic scenarios:

1. Estimate  $\hat{\gamma}$  for each interferometric pair by averaging over the complex-valued pixels.
2. Result: Coherence magnitude,  $|\hat{\gamma}|$ , and phase,  $arg(\hat{\gamma})$ , of the spatial average.
3. Infer  $\Delta m_{ab}$  for each pair using Equation 13 or other function relevant for that distribution of  $s$ .
4. Linear regression for  $s_j$ :  $\hat{s}_j = \frac{1}{N!2!(N-2)!} \sum_{a=1}^{N-1} \sum_{b=a+1}^N \Phi_j(t_a, t_b) / \Delta m_{ab}$

This will not result in the exact value of  $\Delta m$  and  $s$  used in generating the synthetic scenario, because  $s$  is a random variable and the number of samples,  $N$ , is finite, but will approach the input value as  $N$  becomes large. The approach above takes the mean in (4) over all possible interferograms, but a subset could be used as well.

For real-world data, there are other factors that contribute to coherence magnitude, such as surface roughness and permanent changes (e.g., Zebker and Villasenor, 1992). Additionally, contributions to the interferometric phase, including atmospheric variability (e.g., Goldstein, 1995; Emardson et al., 2003; Elliott et al., 2008; Bekaert et al., 2015) and ground displacements (e.g., Massonnet et al., 1993; Lundgren et al., 2004; Bell et al., 2008), will generally be large compared to the soil moisture term discussed in this paper. Therefore, we attempt to find the most suitable coherence magnitude,  $|\hat{\gamma}|$ , and phase,  $arg(\hat{\gamma})$ , associated with soil moisture alone by using the approach outlined below.

### 3.3.1 Coherence magnitude used in correction

For coherence magnitude, we follow a variant of the approach used in Bürgi and Lohman, 2021, where we model the estimate of coherence magnitude for an interferometric pair at a given location as a product of the following four terms:

$$\gamma_{tot} = \gamma_0 \gamma_b \gamma_p \gamma_r \quad \text{Eq. 15}$$

where each  $\gamma$  term indicates coherence magnitude,  $\gamma_{tot}$  is the coherence magnitude estimated over a region (here, 10x10 pixels),  $\gamma_0$  is the “background” coherence due to factors such as surface roughness,  $\gamma_b$  is the portion of the coherence that depends linearly on the perpendicular baseline of the interferogram,  $\gamma_p$  is the “permanent” loss of coherence associated with a given time interval, and  $\gamma_r$  is a term linearly related to the absolute value of the relative difference in a soil moisture metric between the two dates forming the interferogram.  $\gamma_0$  can also be thought of as the highest that coherence ever gets for that location, and  $\gamma_p$  for a given pair of dates is the product of the permanent loss of coherence occurring during all of the intervening time intervals. In the example shown in Figure 3a, it can be seen that permanent coherence loss is very low at this site, since the longest, 2-year pair (upper right corner) is nearly as coherent as the shortest

time-scale pairs. The drops in coherence associated with the precipitation events at this location were not associated with any significant surface changes (erosion, deposition, etc.) that would have changed the scatterer orientation within the pixel and resulted in lower coherence for any pair spanning those time intervals.

Here, we adjust this approach slightly to reflect our new model of the soil moisture effect on coherence. We solve for the time series of  $m_k$  such that  $\gamma_r = E[\widehat{\gamma}]$  using the relationships in Table 1. For example, for exponentially-dependent  $s$ , the predicted coherence magnitude is:

$$\gamma_{tot} = \gamma_0 \gamma_b \gamma_p \frac{1}{(1 + \Delta m^2)^{1/2}} \quad \text{Eq. 16}$$

We solve for the right-hand side factors in Equation 16 using all possible interferometric pairs and a nonlinear trust-region reflective algorithm (e.g., Coleman and Li, 1996) and require that coherence magnitude is bounded between 0 and 1, and that the  $m_k$  are positive. An example of the model parameters and fit to the data at the same pixel as shown in Figure 3a is given in Figure 8, with the baseline dependence shown in Figure 18 in Appendix B.  $\gamma_b$  is small for the data examined in this study, potentially because we focus on high-coherence regions with low relief. The  $m_k$  that result from this inversion are the values that we use in the next sections.

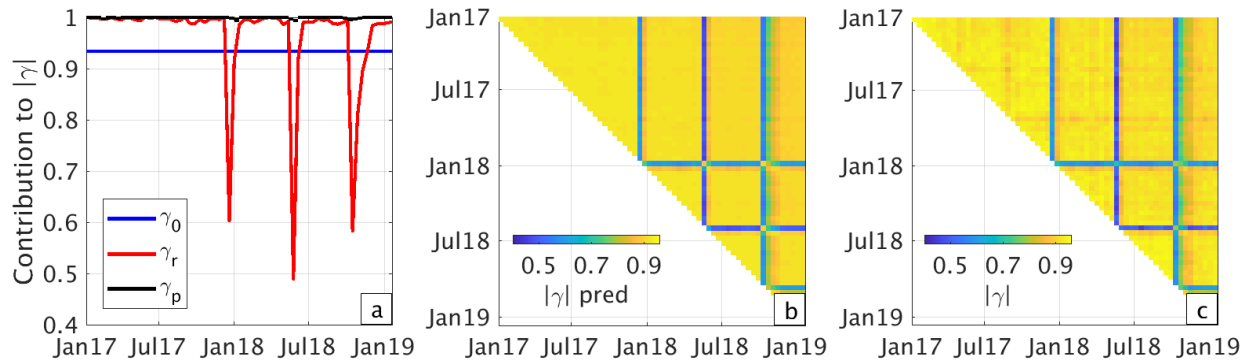


Figure 8: a) Coherence terms inferred at the pixel indicated by the red circle in Figures 1 and 2, and shown in Figure 3 and 4.  $\gamma_b$  depends on the perpendicular baseline of each pair, and is not shown here, see Figure 18 in Appendix B.  $\gamma_r$  for all pairs relative to the first date (red),  $\gamma_0$  (time-invariant, blue), and the small values of permanent change,  $\gamma_p$  (black). b) Predicted coherence from four terms in Eqs 15 and 16. c) Input coherence.

### 3.3.2 Phase used in correction

To correct for the effects of soil moisture on phase, we need to infer the portion of the observed interferometric phase that is due to soil moisture for the interferograms used in solving for  $s_j$  at each pixel. The phase of the full-resolution interferogram will contain contributions from the

soil-moisture-based component of the phase,  $\phi_j^{sm}$ , as well as from variations in atmospheric properties, ground displacement, and other changes in surface properties.

$$\psi_j(t_b, t_a) = \psi_j^{sm}(t_b, t_a) \psi_j^{atm}(t_b, t_a) \psi_j^{disp}(t_b, t_a) \psi_j^{noise}(t_b, t_a) \quad \text{Eq. 17}$$

where,  $\psi_j^{sm}(t_b, t_a) = e^{i\phi_j^{sm}}$  is the soil moisture term,  $\psi_j^{atm}(t_b, t_a)$  is due to variations in atmospheric properties,  $\psi_j^{disp}(t_b, t_a)$  is due to ground displacement, and  $\psi_j^{noise}(t_b, t_a)$  includes all other types of noise and signals. If the atmospheric and displacement signals have large spatial scales compared to the spatial scale of the averaging used to estimate  $\hat{\gamma}_j(t_b, t_a)$ , then their contribution to the phase of  $\hat{\gamma}_j(t_b, t_a)$  will approach a constant value over the averaging window. Note that below we equate the complex coherence with the filtered interferogram,  $\hat{\gamma}_j(t_b, t_a) = \overline{\psi_j}(t_b, t_a)$ . If we assume that the spatial average of the other noise terms,  $\overline{\psi_j^{noise}}(t_b, t_a)$ , approaches zero as  $N$  increases, then we have:

$$\hat{\gamma}_j(t_b, t_a) = \overline{\psi_j^{sm}}(t_b, t_a) \overline{\psi_j^{large}}(t_b, t_a) \overline{\psi_j^{noise}}(t_b, t_a) \approx \overline{\psi_j^{sm}}(t_b, t_a) \overline{\psi_j^{large}}(t_b, t_a) \quad \text{Eq. 18}$$

where  $\overline{\psi_j^{large}}(t_b, t_a)$  is the spatial average of the atmospheric and displacement terms with large spatial scales. Since we previously solved for the time series of  $m_k$ , we can infer  $\overline{\psi_j^{sm}}(t_b, t_a)$  from the values in Table 1 using our assumed probability distribution for  $s$ . For the exponential distribution,  $E\left[\arg\left(\overline{\psi_j^{sm}}(t_b, t_a)\right)\right] = \tan^{-1}\Delta m_{ab}$ , and Equation 18 becomes:

$$\hat{\gamma}_j(t_b, t_a) \approx e^{i \tan^{-1}\Delta m_{ab}} \overline{\psi_j^{large}}(t_b, t_a) \quad \text{Eq. 19}$$

Rearranging terms:

$$\overline{\psi_j^{large}}(t_b, t_a) \approx \hat{\gamma}_j(t_b, t_a) e^{-i \tan^{-1}\Delta m_{ab}} \quad \text{Eq. 20}$$

We approximate the full-resolution, soil-moisture-derived component of the interferogram,  $\widehat{\psi_j^{sm}}(t_b, t_a)$ , by multiplying the full-resolution, uncorrected interferogram,  $\psi_j(t_b, t_a)$ , by the complex conjugate of the larger-spatial-scale terms from the right-hand side of Eq. 20:

$$\widehat{\psi_j^{sm}}(t_b, t_a) = \psi_j(t_b, t_a) \overline{\overline{\psi_j^{large}}(t_b, t_a)}^* \approx \psi_j(t_b, t_a) \hat{\gamma}_j(t_b, t_a)^* e^{i \tan^{-1}\Delta m_{ab}} \quad \text{Eq. 21}$$

The first part of the right-hand term,  $\psi_j(t_b, t_a) \hat{\gamma}_j(t_b, t_a)^*$ , is a high-pass filtered version of the full resolution interferogram. The phase that we attribute to soil moisture,  $\arg(\widehat{\psi}_j^{sm}(t_b, t_a))$ , is therefore the high-pass filtered phase (Figure 3b), with an additional correction for the mean value through the  $\tan^{-1} \Delta m_{ab}$  term.

Using the approach described above, we calculate the complex coherence and solve for  $\Delta m_{ab}$  and  $\phi_j^{sm}(t_b, t_a)$ . In this dataset, we have sixty dates with little precipitation and only three with strong soil moisture signals. To avoid having the high-coherence, “dry” dates dominate the inversion for  $s_j$  at each pixel, we introduce two additional steps. Firstly, we estimate the phase as a function of time that best fits the full set of high-pass filtered interferograms (Figure 3c, Appendix C). We then solve for the best fit  $s_j$  using that phase model and the time series of  $m_k$ , weighting our inversion by  $m_k$  to further enhance the contribution of the time periods impacted by precipitation. We then correct the phase at each pixel for each interferogram as:

$$\psi_j^{corrected}(t_b, t_a) = \psi_j(t_b, t_a) e^{-i(\Delta m_{ab} s_j)} \quad \text{Eq. 22}$$

where  $s_j$  is the slope solved for in the previous step. In Section 4 we show the results of this correction on coherence magnitude and phase closure. We also performed the same approach using the original interferograms (instead of the phase model vs. time), but found that the improvement in coherence was lower by around 30% and the computational cost was higher.

In areas with a large amount of permanent decorrelation and/or surface change, the assumptions made above will break down. Additionally, this approach assumes that the underlying statistical distribution of  $s$  is close to the ones from Table 1 that we use in estimating both  $\Delta m_{ab}$  and  $\phi_j^{sm}(t_b, t_a)$ . Below, we ignore these potential sources of error, but they likely contribute to the residual coherence magnitude features present in our data after correction.

## 4.0 Results

Here we show the results of using the exponential distribution,  $\Gamma(1, 1)$  (Table 1).

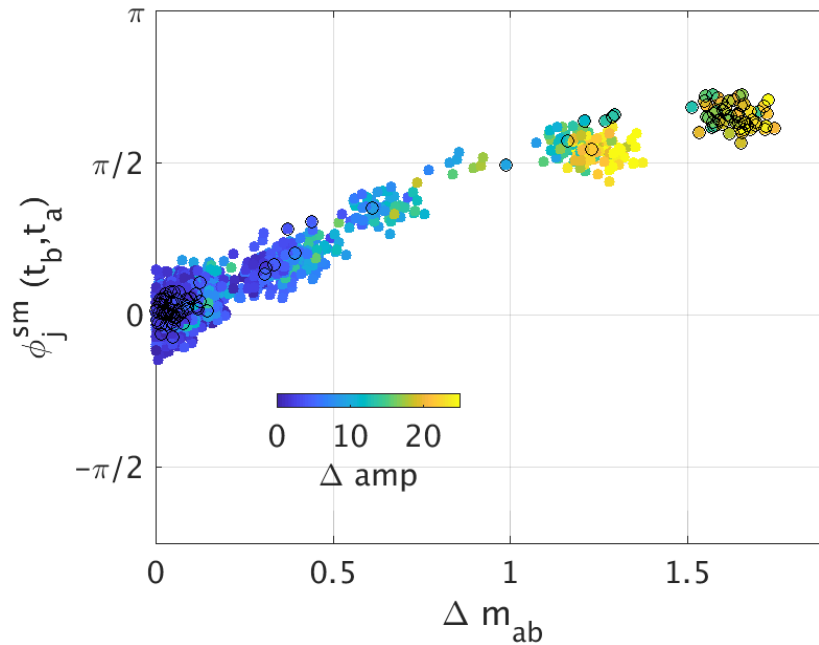


Figure 9: Soil moisture component of phase of all possible pairs,  $\phi_j^{sm}(t_b, t_a)$  vs.  $\Delta m_{ab}$  for the  $\Gamma(1, 1)$  distribution, at pixel indicated by red dot in Figures 1 and 2. Color as in Figure 3c. Black outline indicates pairs that include either 2018/05/14 or 2018/05/26, dates that are not used in the inversion for  $s$ . For clarity,  $\phi_j^{sm}(t_b, t_a)$  and  $\Delta m_{ab}$  are multiplied by the sign of  $\Delta m_{ab}$  to emphasize the near-linear relationship (pairs with negative  $\Delta m_{ab}$  would otherwise plot in the lower left quadrant)..

In order to check on whether any improvements in coherence are truly independent of the filtering and estimation steps applied to the set of interferograms, we solve for the value of  $s_j$  at each pixel without using any interferograms that include the dates 2018/05/14 or 2018/05/26, which are the dates that most closely bracket the second precipitation event. For the pixel examined here,  $s = 1.27$  (Figure 9).

In Figure 10, we show the complex coherence magnitude, high-pass filtered phase and phase closure, using the same approaches used in generating Figures 3 and 4, but using the corrected interferograms instead of the original interferograms. Note that the coherence magnitude (Figure 10a) is closer to unity, although there is still lower coherence associated with the precipitation events. Similarly, phase closure values are much smaller, although there is still a bias associated with each precipitation event.

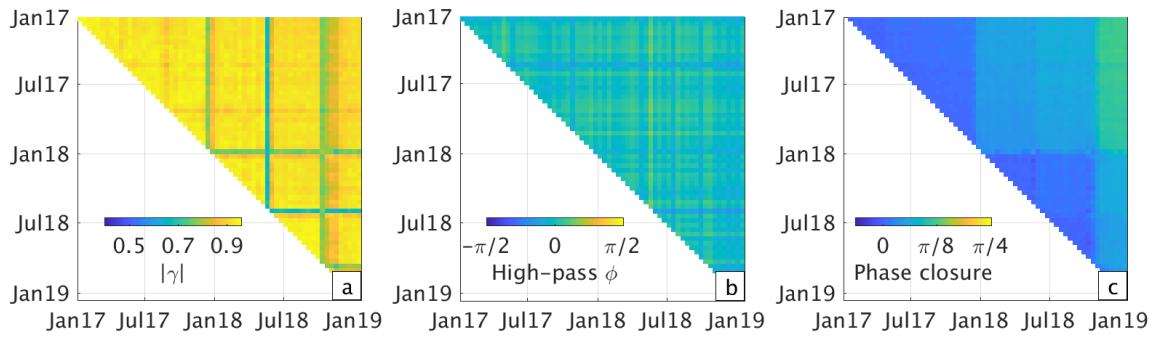


Figure 10: Phase characteristics at same point shown in other figures, after correction. Color scales are the same as in Figures 3 and 4. a) Coherence magnitude for all possible pairs of dates. b) High-pass filtered phase, using a Gaussian window with width and length 10 pixels. c) Phase closure for all possible  $T_{12}(t_a, t_b)$  for the 63 dates in the Sentinel-1 timeseries.

When we compare the coherence before and after the correction for only the 2018/05/14-2018/05/26 interferogram within the full region indicated by the blue box in Figures 1 and 2 we can see that the region where rain fell during Typhoon Mekunu is associated with an improvement in coherence, while the regions with no rain are unaffected (Figure 11).

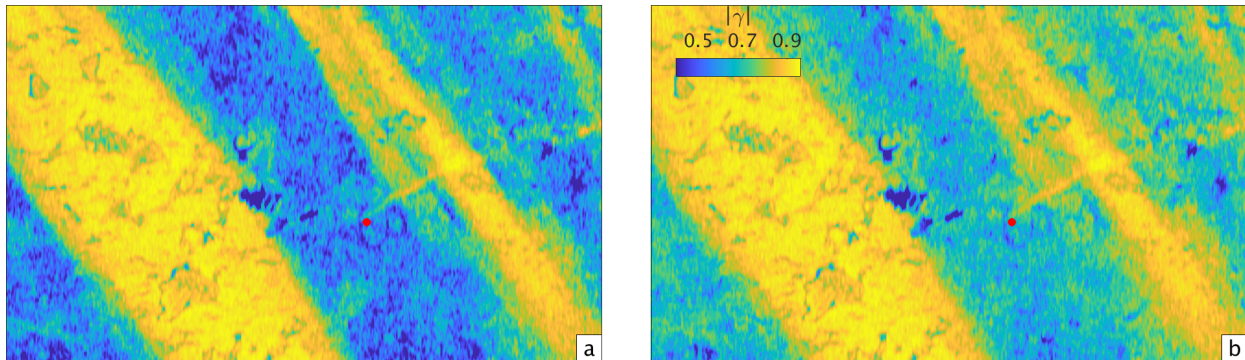


Figure 11: Coherence magnitude before (a) and after (b) correction for pair 2018/05/14-2018/05/26, using the exponential distribution ( $\Gamma(1, 1)$ ) as a model. All dates except these two dates were used in generating the model parameters used in this correction. Location of point shown in Figure 10 and previous figures is indicated by red circle.

Histograms of the original data and results of corrections using the two types of asymmetric distributions for  $s$  listed in Table 1 show that there is not a significant difference between the two approaches (Figure 12), although the  $\Gamma(1, 1)$  distribution (i.e., the exponential distribution) fits the data slightly better, including less of a decrease in coherence within the high-coherence areas that were unaffected by rain (rightmost peak in Figure 12).

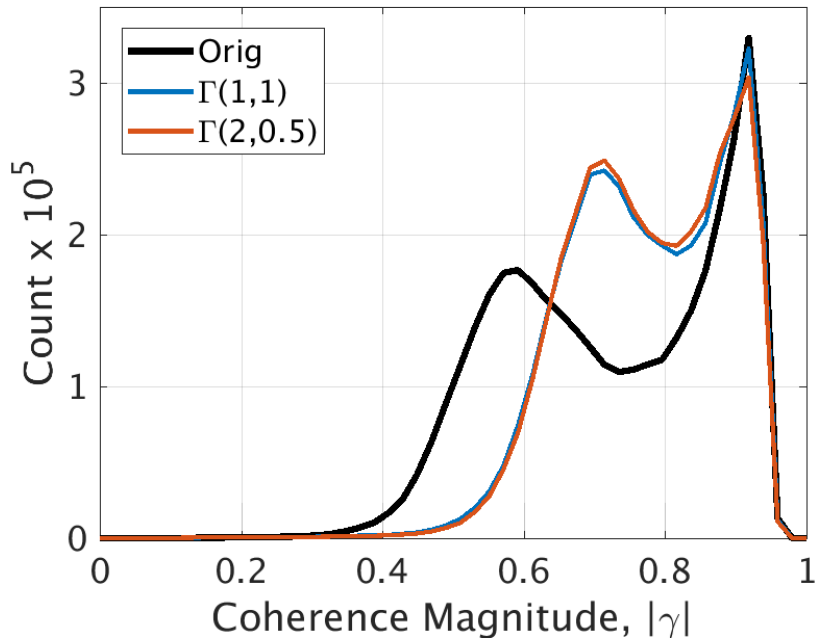


Figure 12: Histogram of coherence improvement. Original coherence (black) and coherence magnitude after corrections using the  $\Gamma(1, 1)$  (blue) and  $\Gamma(2, 0.5)$  (red) approaches from Table 1.

## 5.0 Discussion and Conclusions

This study region is marked by unusually high interferometric phase stability. We are able to isolate the temporary effects on phase and coherence associated with precipitation and distinguish them from other factors affecting the SAR data because of the high “background” coherence and because of the long dry intervals between storms that allow us to observe how the coherence for pairs spanning the event evolves over time. In many areas of the world where the effects of soil moisture on InSAR targets of interest (e.g., agricultural areas), this analysis may not be possible, particularly during time periods of rapid surface change (e.g., plowing, harvests, rapid vegetation growth). However, during time periods where interferometric coherence magnitude is high, unless the SAR signal is completely dominated by volume scattering within the vegetation, the processes observed here likely contribute to the data to some degree.

Even in areas with intensive agriculture, such as central California, many fields are left fallow at any given time. Studies of subsidence associated with groundwater withdrawal or other subsurface deformation sources in these regions (e.g., Lyons et al., 2002; Farr et al., 2016; Murray and Lohman, 2018; Jiang and Lohman, 2021; Neely et al., 2021) would be impacted by soil moisture signals of the sort inferred here, resulting in potential biases in the rates or other parameters derived from a time series of filtered/downsampled interferograms (Figure 7). Nonzero closure phase, which is consistent with a soil moisture effect of the sort described here, has been seen extensively in many areas of the world (e.g., Zwieback et al., 2016; De Zan and

Gomba, 2018; Michaelides and Zebker, 2019; Benoit et al., 2020; Zheng et al., 2022). While the approach described here may not be applicable everywhere, the synthetic tests described in Section 3.2 could potentially be used to constrain the potential magnitude of errors that could be introduced by unmodeled soil moisture changes.

In this paper we do not go so far as to convert the metric for soil moisture,  $m_k$ , into a more meaningful constraint on volumetric soil moisture. Unfortunately, there are no *in situ* observations of soil moisture in the region examined here, although we have previously compared the temporal behavior of coherence magnitude changes and its recovery time to other independent models and observations (Bürgi and Lohman, 2021). The requirement for long SAR time series and the generation of all possible pairs also presents some challenges for operational use of this approach. However, the repeatability of the coherence and phase changes that we see in this area give us hope that this approach could be adapted for use in quantifying soil moisture in other environments where there is little vegetation. As an example, once several precipitation events have been observed and a model of the spatial distribution of soil moisture sensitivity,  $s_j$ , has been determined, the high-pass filtered version of a subsequent interferogram could be compared against that distribution, and the spatial correlation with  $s_j$  could potentially serve as an initial estimate of the soil moisture metric,  $m_k$ , even without the re-processing of earlier pairs. Processes that permanently affect the distribution of scatterers within a pixel, such as transport or deposition by flooding or wind, would not likely correlate with the previous distribution of  $s_j$  on a pixel-to-pixel basis. By the same token, an initial correction to the interferometric phase (e.g., for use in ground deformation analyses) could also be performed. Our examples where we solve for  $s_j$  using all dates except for 2018/05/14 and 2018/05/26 and then apply the correction to those dates is similar to this proposed approach except for the fact that the unused dates were in the middle of the time series and, therefore, we also have information about coherence returning to “normal” for longer-term pairs spanning that time interval. In the case of dates at the end of the time series, it will be less apparent whether changes in coherence are due to permanent change or soil moisture.

Upcoming SAR missions, such as the NASA-ISRO SAR mission (NISAR, (e.g., Rosen et al., 2017), will add to the temporal and spectral diversity of the available SAR data catalog and facilitate studies in regions where large amounts of ongoing surface change have impeded previous studies. In all likelihood, signals such as the ones observed in the dataset presented in this paper will become more common and need to be addressed or better understood if we are to separate out the effects of ground displacement from other factors affecting the data. Additionally, the increasing precarity of water sources globally (e.g., Green et al., 2011; Gleeson et al., 2012; Bierkens and Wada, 2019; Gleeson et al., 2020) motivates the need for more observations of surface hydrology and water use, including variations in soil moisture.

In conclusion, we observe that, in this region, the phase of a given pixel tends to change with respect to its neighbors in the same manner each time it rains. We present a simple statistical

model describing the pixel-to-pixel variability in the strength of the response to soil moisture changes, and show that this model predicts behaviors in the spatially averaged or filtered phase that are observed in real data. We also show that corrections used based on this model improve the coherence magnitude of an interferogram affected by soil moisture, even when those particular dates are not used to solve for the best-fit value of  $s_j$ . Future work examining locations where *in situ* observations of soil moisture are available would help determine whether this approach could be relevant to the study of volumetric soil moisture as well. Synthetic tests such as the ones performed in Section 3.2 could also help predict the magnitude of expected changes and aid in the interpretation of any observed signals.

## Acknowledgements

This work was supported by NESSF fellowship #80NSSC17K0385 and NASA grant #NNX16AL20G. Copernicus Sentinel data from 2017-2019 were retrieved from ASF DAAC in 2019, processed by ESA. Figures were prepared using PyGMT and Matlab, and Landsat-8 imagery is provided courtesy of the U.S. Geological Survey.

## Appendix A

### A.1 Synthetic scenarios: 3 pixels, 3 dates

As described above and elsewhere in the literature (e.g., De Zan et al., 2015; Gruber et al., 2016; Zwieback et al., 2016), nonzero phase closure stems from the fact that spatial averaging of a set of complex-valued InSAR observations is nonlinear. The spatially-averaged or filtered complex interferograms will generally have a different phase than the average of the unwrapped, real-valued phase of that same set of pixels. We can demonstrate this, and evaluate the magnitude of the effect of filtering, downsampling and corrections, using simple cases with synthetic data with as few as three pixels and three dates. We begin by showing the effect of spatial averaging on a single interferogram between two dates, and then expand to the triplet phase closure problem between three dates.

For this example, we compute the average over three pixels using data from three dates (i.e., nine total full-resolution phase values), and simplify further by making all of the complex-valued observations be unit vectors. We also fix the phase as zero for all but one of the three pixels. Only the first pixel on the second and third dates has non-zero phase in this example. For the first date, all pixels have zero phase.

Even in this simple example,  $\overline{\Phi}^{wrap}(t_a, t_b)$  differs from  $\overline{\Phi}^{true}(t_a, t_b)$ . When we average over all three pixels, the estimate of the complex coherence between the first two dates is:

$$\hat{\gamma}(t_2, t_1) = \frac{1}{3} \sum_{j=1}^3 \psi_j(t_2, t_1) = \frac{1}{3} \sum_{j=1}^3 u_j(t_2) u_j(t_1)^* = \frac{1}{3} \sum_{j=1}^3 e^{i\phi_j(t_2)} e^{-i\phi_j(t_1)} = \frac{1}{3} \sum_{j=1}^3 e^{i(\phi_j(t_2) - \phi_j(t_1))} \quad \text{Eq. A1}$$

Because  $\phi_j(t_k) = 0$  everywhere except for at  $j=1$  and  $k=2,3$ :

$$\hat{\gamma}(t_2, t_1) = \frac{1}{3} (e^{i(\phi_1(t_2) - 0)} + e^0 + e^0) = \frac{1}{3} (\cos(\phi_1(t_2)) + i \sin(\phi_1(t_2)) + 1 + 1) \quad \text{Eq. A2}$$

The phase of the resulting spatially averaged, wrapped interferogram over these three points and two dates is therefore:

$$\bar{\Phi}^{wrap}(t_2, t_1) \equiv \arg(\hat{\gamma}(t_2, t_1)) = \text{atan}(\sin(\phi_1(t_2)), (2 + \cos(\phi_1(t_2)))) \quad \text{Eq. A3}$$

which differs from the average of the “true” pixel values,  $\bar{\Phi}^{true}(t_2, t_1)$ :

$$\bar{\Phi}^{true}(t_2, t_1) \equiv \frac{1}{3} \sum_{j=1}^3 \arg(\psi_j(t_2, t_1)) = \frac{1}{3} (\phi_1(t_2) + 0 + 0) = \frac{1}{3} \phi_1(t_2) \quad \text{Eq. A4}$$

For  $\phi_1(t_2) = 120^\circ$ ,  $\bar{\Phi}^{true}(t_2, t_1) = 120^\circ/3 = 40^\circ$  and  $\bar{\Phi}^{wrap}(t_2, t_1) = 30^\circ$  (Figure A1). As  $\phi_1(t_2)$  increases, the difference between  $\bar{\Phi}^{true}$  and  $\bar{\Phi}^{wrap}$  increases as well, up to a maximum of 60 degrees at  $\phi_1(t_2) = \pi$  (Figure A1b). Note that the length of the average vector (Figure A1a, green) decreases as  $\phi_1(t_2)$  increases, down to a minimum of  $1/3$  when  $\phi_1(t_2) = \pi$ . The length of this vector is similar to the coherence magnitude,  $|\gamma|$ , and is a measure of the scatter of the phase values around their mean.

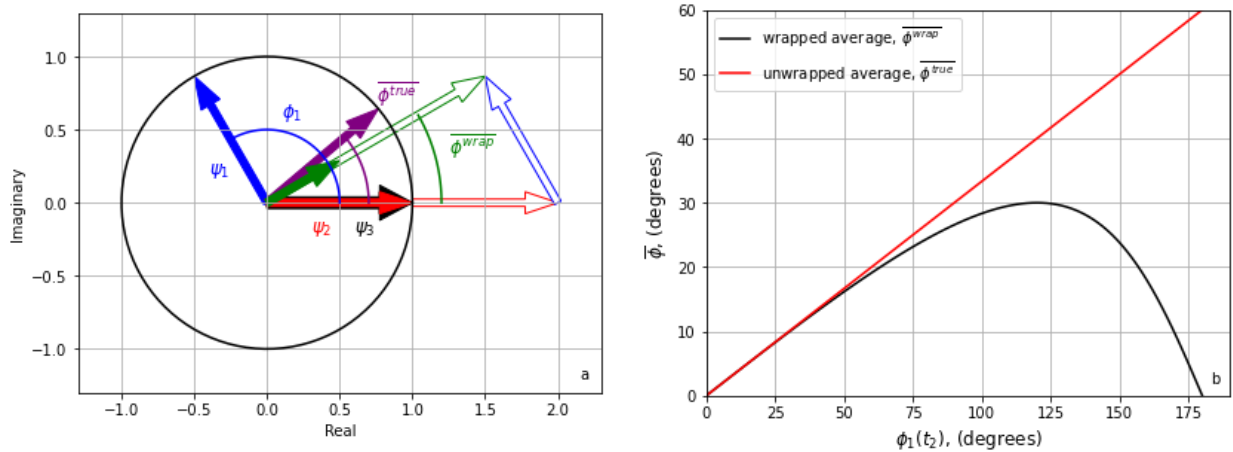


Figure A1: Synthetic scenario between two dates and three pixels. a) Vector representation of interferograms between the first and second dates at the  $j = 1, 2, 3$  pixels (solid blue, red and black

arrows,  $\psi_j$ , note that  $\psi_2$  and  $\psi_3$  overlap and are equivalent). The only non-zero phase value is  $\phi_1(t_2) = 120^\circ$  on the 2nd date (blue). Purple indicates a vector with phase equivalent to the average of the “true”, or unwrapped phase values,  $\bar{\Phi}^{true}(t_2, t_1) = 40^\circ$ . Outlined vectors have the same magnitude and orientation as the  $\psi_j$ , and show graphically the complex-valued sum/average of the three interferograms, with phase  $\bar{\Phi}^{wrap}(t_2, t_1) = 30$  (green arrow, open and filled, respectively). The thin black line indicates the unit circle. b) Difference between  $\bar{\Phi}^{true}$  and  $\bar{\Phi}^{wrap}$  for values of  $\phi_1(t_2)$  between  $0$  and  $180^\circ$ .

The same effects are present when we allow the phase of the second pixel,  $\phi_2(t_2)$ , to vary as well. If  $\phi_2(t_2)$  varies between the values of the other two pixels, with  $\phi_2(t_2) = r \phi_1(t_2)$ , and  $r$  ranging between  $0$  and  $1$  (Figure A2). In Figure A2c, we see that  $\bar{\Phi}^{true}$  is equal to  $\bar{\Phi}^{wrap}$  only when  $\phi_2(t_2)$  is exactly halfway between the other two vectors ( $r = 0.5$ ), or when the phase is zero for all three points. In general, for any given interferogram where we average spatially, the difference between the wrapped and unwrapped phase average is larger when the phase values are not distributed symmetrically around their mean.

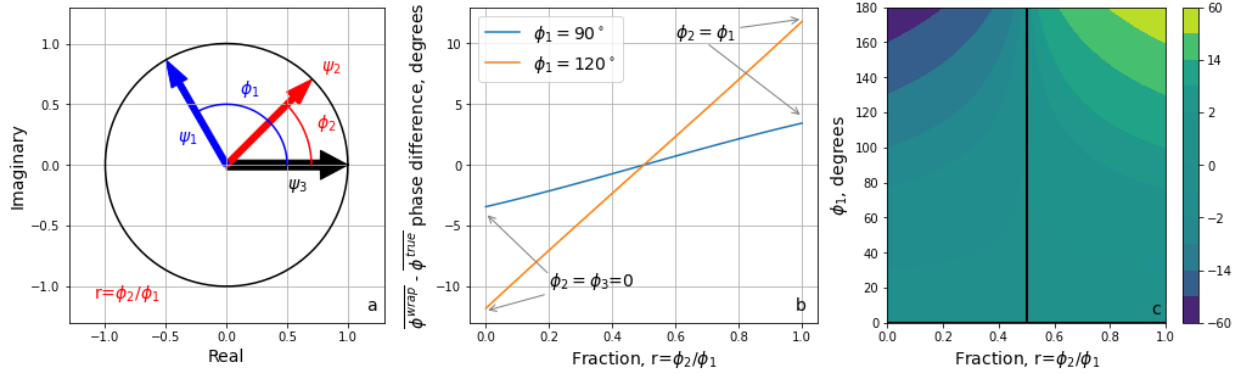


Figure A2: Same synthetic scenario, but with  $\phi_2(t_2) = r \phi_1(t_2)$ . a) Vector representation. b) Effect on  $\bar{\Phi}^{wrap} - \bar{\Phi}^{true}$  for  $\phi_1(t_2) = 90^\circ$  and  $120^\circ$ . c) Effect on  $\bar{\Phi}^{wrap} - \bar{\Phi}^{true}$  (color, degrees) for all values of  $\phi_1(t_2)$  between  $0$  and  $180^\circ$  and for all values of  $r$  between  $0$  and  $1$ . Black line indicates  $\bar{\Phi}^{wrap} = \bar{\Phi}^{true}$ , which is true for  $r=0.5$  and for  $\phi_j(t_2)=0$  for all  $j$ .

The previous two figures involved spatial averaging of just one interferogram between two dates. When the third date is also examined, we can evaluate the dependence of triplet phase closure on the phase of the three pixels included in the average. As shown in Figure A2, the averaging effects will be zero when the pixels have phase values that are evenly spaced (i.e.,  $r = 0.5$ ). For larger numbers of pixels, this is similar to the scenario where the phase values are evenly distributed about the mean/median, such as you would find for a normal distribution.

The triplet phase closure,  $\tau_{abc}$  (Eq. 4), between the three averaged interferograms in our scenario depends on the phase values of the first pixel on the second two dates,  $\phi_1(t_2)$  and  $\phi_1(t_3)$  and how much they differ from each other. When any two of the phase values are equivalent, the triplet phase closure error is zero (Figure A3)

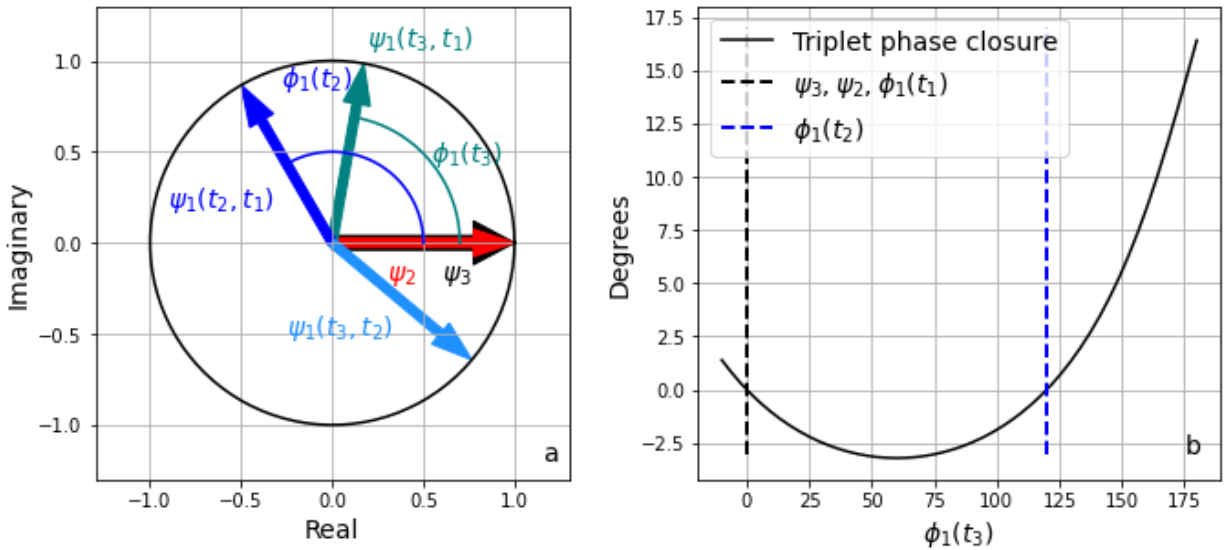


Figure A3: Scenario for three points and three dates. a) Vector representation for  $\phi_1(t_2) = 120^\circ$  and  $\phi_1(t_3) = 80^\circ$ , with the interferograms at pixel one for the three possible pairs between dates:  $t_2 - t_1$  (dark blue),  $t_3 - t_1$  (teal) and  $t_3 - t_2$  (light blue). Interferograms for pixels 2 and 3 are still zero, as in previous examples (red and black arrows) b) Triplet phase closure  $\tau_{123}$  vs. phase at pixel 1 on third date (solid black curve), for  $\phi_1(t_2) = 120^\circ$  (dashed blue curve). Note that triplet is zero when  $\phi_1(t_3)$  is equal to the phase on either of the first or second dates.

To summarize the results of these 3-point, constant amplitude scenarios, we find that non-zero triplet phase closure occurs when the two following conditions hold. First, on a given date, the phase values within the region where averaging/filtering is applied are not evenly distributed around their mean. Secondly, the perturbation to the spatially averaged phase has to persist over time - i.e., for three dates, two of the dates can not have the same value. For soil moisture, this is similar to the case where a precipitation event occurs and the soil dries out partially, but not completely, by the next observation.

## A.2 Synthetic scenarios: N pixels, 3 dates

In Figure A4 we show the differences in spatially averaged wrapped and unwrapped phase for interferograms between a “dry” date and a second date within a range of  $m_2$ , where the  $s_j$  values are drawn from either a normal distribution or exponential distribution. Since  $m_1 = 0$ ,

this means that  $\Delta m_{12} = m_2$ . The associated values of  $|\hat{\gamma}|$  are shown as well (Eq 12). Confidence intervals shown represent the range of values expected for averaging over 100 pixels - spatial averages over smaller numbers of pixels would have larger variability. The expected value of the phase average with normally-distributed  $s_j$  (blue line) is the same as the true unwrapped phase average (black lines), although there is some variability between iterations due to the fact that this average is computed over a finite number of pixels.

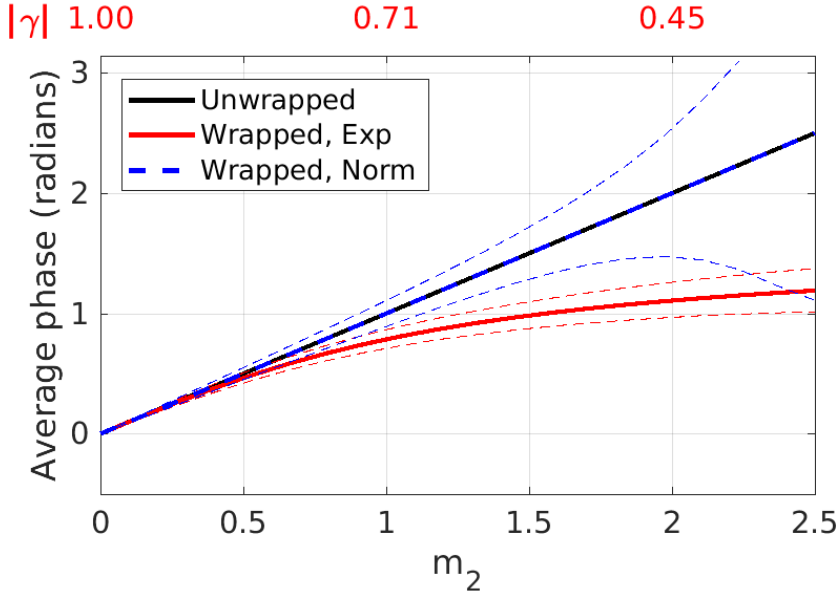


Figure A4: Scenario for averaging of 100 points for interferograms between a dry date ( $m_1=0$ ) and values of  $m_2$  ranging between 0 and 2.5 for the 2nd date. Black curve indicates the average of the unwrapped exponentially distributed noise and the red curve indicates the average of the complex-valued wrapped phase. Blue curve indicates the average of normally-distributed  $s$  with the same variance. Dashed lines indicate the 68% confidence intervals after  $10^5$  trials. Corresponding values of  $|\hat{\gamma}|$  for the pair are shown along the x-axis at the top of the graph.

For the data with exponentially-distributed  $s_j$ , we can use the relationships in Table 1 to show that the phase triplet between three dates with different values of  $m_k$  has an expected value of:

$$\hat{\gamma}_j(t_2, t_1) \hat{\gamma}_j(t_3, t_2) \hat{\gamma}_j(t_1, t_3) = e^{i \tan^{-1}(\Delta m_{12})} e^{i \tan^{-1}(\Delta m_{23})} e^{i \tan^{-1}(\Delta m_{31})} = e^{i(\tan^{-1}(\Delta m_{12}) + \tan^{-1}(\Delta m_{23}) + \tan^{-1}(\Delta m_{31}))}$$

Eq. A5

If any two of the  $m_k$  are equivalent to one another, the phase triplet error becomes zero. If we fix  $m_1 = 0$  and vary  $m_k$  for the other two dates (Figure A5), we have:

$$\hat{\gamma}_j(t_2, t_1) \hat{\gamma}_j(t_3, t_2) \hat{\gamma}_j(t_1, t_3) = e^{i(\tan^{-1}(m_2) + \tan^{-1}(m_3 - m_2) - \tan^{-1}(m_3))}$$

Eq. A6

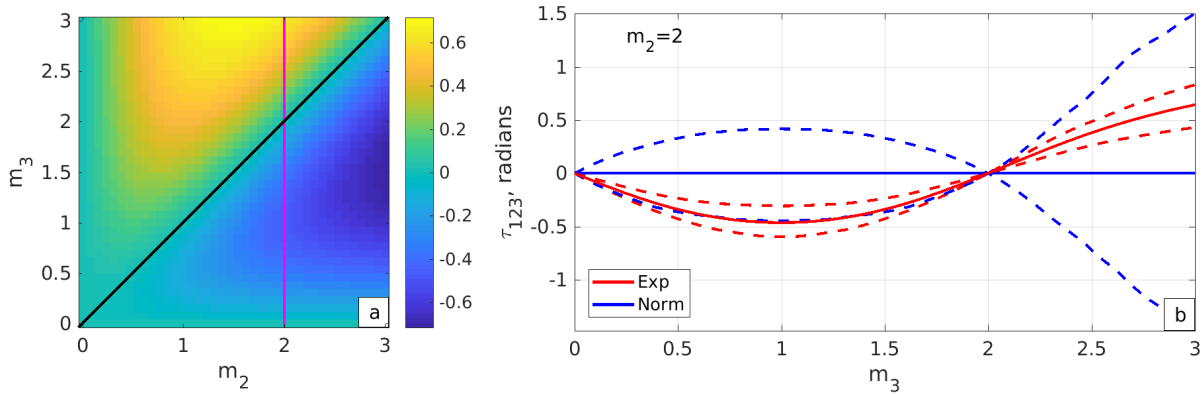


Figure A5: a) Expected value of triplet phase when  $m_1=0$ , for  $m_2$  and  $m_3$  ranging between 0 and 5. Black line indicates where  $m_2 = m_3$ , resulting in zero triplet phase. Magenta line indicates profile shown in (b). b) Profile of triplet phase error with exponentially-distributed  $s$  (red) for  $m_2 = 2$  and a range of  $m_3$ , with 68% confidence limits. Blue indicates errors for normally-distributed  $s$  with same variance and mean as the unwrapped soil moisture phase,  $s_j m_k$ , for each value of  $m_k$ . Scenario averages over 100 points and confidence limits reflect  $10^4$  trials.

Note that, as expected, whenever  $m_2$  or  $m_3 = 0$ , and are, therefore, equivalent to  $m_1$  in this scenario, the triplet phase is zero. It is also zero when  $m_2 = m_3$ .

## Appendix B

For the pixel indicated by the red circle in Figure 1, and in more detail in Figures 3-4, we find that the dependence of coherence on the perpendicular baseline is quite low (Figure A6).

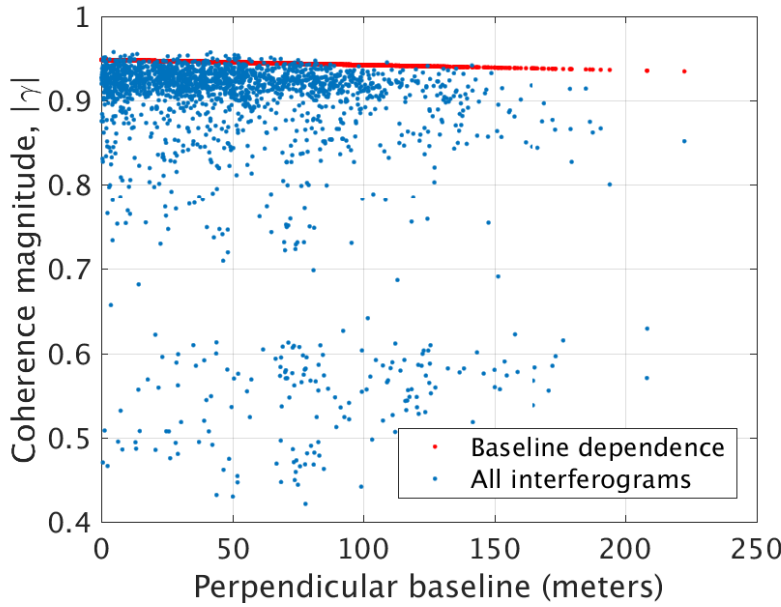


Figure A6: Coherence magnitude vs. the absolute value of the perpendicular baseline for all possible pairs, and best fit line using a robust maximum estimator (Lange et al., 2014).

## Appendix C

For the results shown in this paper, we first invert for a model of phase vs. time on each date, rather than using the interferograms from every possible pair. If computational expense is no object, we can perform a nonlinear optimization for the distribution of phase over time that best-fits the observed phase. However, because the region studied here has such high coherence, and due to the fact that we only observe three episodes of precipitation separated by months-long dry periods, we find that the following approximation works well. We start by solving for the mean complex-valued vector,  $C_0(t_k)$ , of all pairs that include a given SAR observation on each date,  $t_k$ .

$$C_0(t_k) = \frac{1}{63-1} \left[ \sum_{l=1}^{k-1} \widehat{\Psi}_j^{sm}(t_l, t_k) + \sum_{l=k+1}^{63} \widehat{\Psi}_j^{sm}(t_l, t_k) \right] \quad \text{Eq. A7}$$

Where  $\widehat{\Psi}_j^{sm}(t_l, t_k)$  is the estimate of the phase change associated with soil moisture from Equation 21. Figure A7a and A7b illustrate this process- we effectively “flip” the triangular phase diagram shown in Figure 3b along the diagonal and take its complex conjugate. The first iteration of our phase model,  $C_0(t_k)$ , is the phase of the complex-valued average over the rows of Figure A7a.

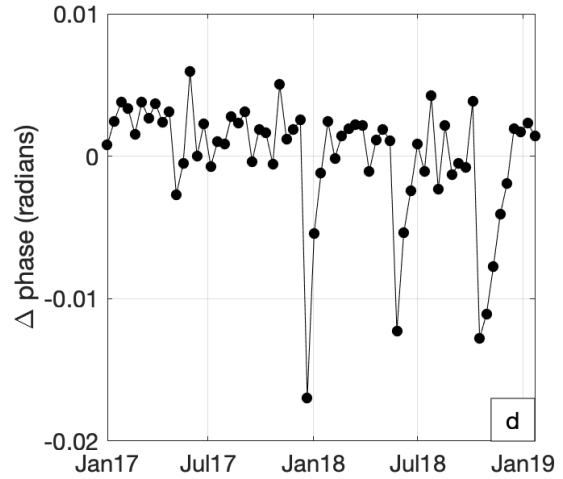
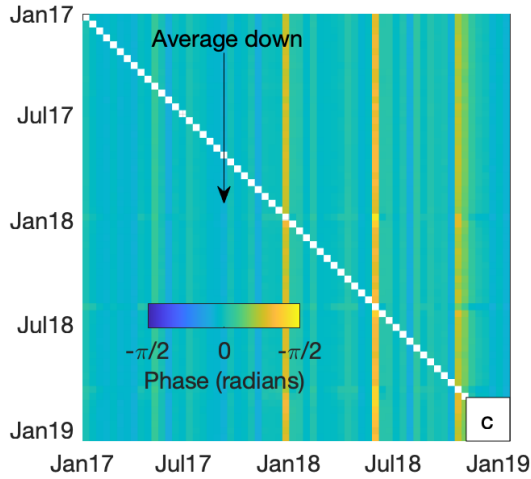
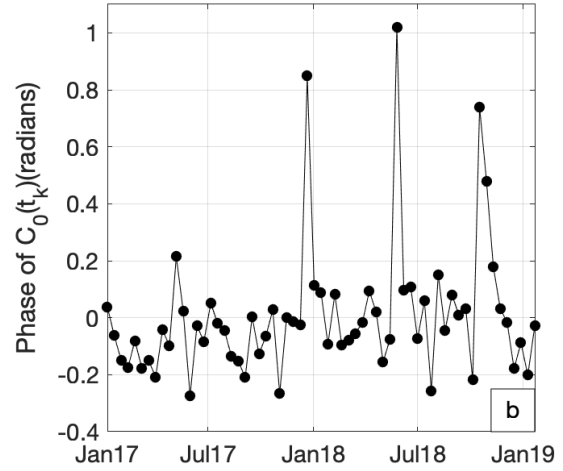
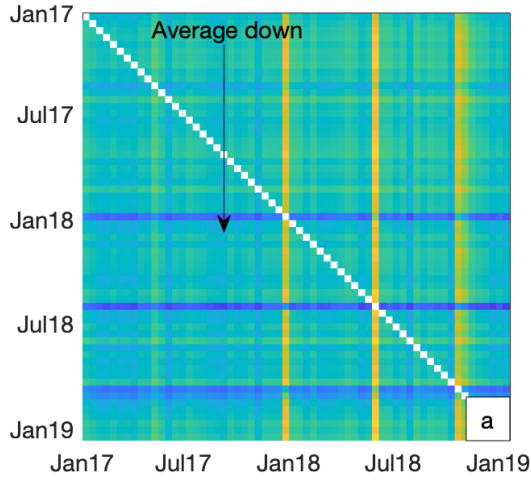


Figure A7 Diagram illustrating iterative process for obtaining phase model at each point. a) High-pass filtered phase (upper right is same as Figure 3c, lower left is the complex conjugate). White along the diagonal indicates the interferograms between a date and itself, which are not used. b) Initial phase model, after averaging over each column of (a). c) Same as (a), but with the model from (b) added to each column. d) Difference between initial model  $C_0$  and final model,  $C$ .

$C_0(t_k)$  is similar to the time series of phase for all pairs vs. the first date (the top row), but includes the benefit of averaging across multiple pairs. However, the results for dates with no precipitation (e.g., most of 2017) are still slightly impacted, as can be seen by the negative (blue) values along the rows associated with the three precipitation events. For the second iteration, we attempt to mitigate this effect by correcting each row with the initial model,  $C_0(t_k)$ .

$$C(t_k) = \frac{1}{63-1} \left[ \sum_{l=1}^{k-1} \widehat{\Psi}_j^{sm}(t_l, t_k) C_0(t_l) + \sum_{l=k+1}^{63} \widehat{\Psi}_j^{sm}(t_l, t_k) C_0(t_l) \right] \quad \text{Eq. A8}$$

Figure A7c illustrates these steps, with the columns associated with “dry” dates now showing no apparent change during the precipitation time periods. In Figure A7d we compare the phase models from the first and 2nd iteration, which differ by only a few %. Figure A8 shows the predictions of this phase model, which closely match the input data. If we examine the residuals (e.g., Figure A8b vs. Figure A8c), we find that there is about a 5% improvement using this approach over what we would have if we simply used the top row (interferograms relative to the first date) as our phase model.

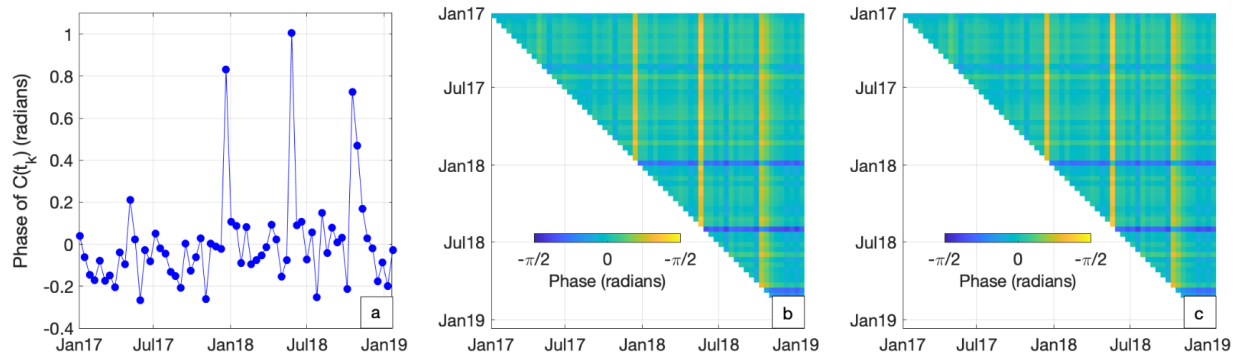


Figure A8 a) Final phase model,  $C(t_k)$ , b) original set of high-pass filtered interferograms (same as Figure 3b) and c) predictions from (a).

At this location, a fully nonlinear inversion for the phase that minimizes the residual between the model and observations only results in an improvement of 0.05%, with a large additional computational cost that would scale with the size of the region and length of the time series. At pixels where the sensitivity to soil moisture,  $s_j$  is small relative to the noise or other signals associated with land surface change, the effect of any errors in this model will not significantly impact our overall result, as a small value of  $s_j$  means that the soil moisture correction will also be small.

## References

- Barrett, B.W., Dwyer, E., Whelan, P., 2009. Soil Moisture Retrieval from Active Spaceborne Microwave Observations: An Evaluation of Current Techniques. *Remote Sens.* 1, 210–242. <https://doi.org/10.3390/rs1030210>
- Bartalis, Z., Wagner, W., Naeimi, V., Hasenauer, S., Scipal, K., Bonekamp, H., Figa, J., Anderson, C., 2007. Initial soil moisture retrievals from the METOP-A Advanced Scatterometer (ASCAT). *Geophys. Res. Lett.* 34.
- Bekaert, D.P.S., Walters, R.J., Wright, T.J., Hooper, A.J., Parker, D.J., 2015. Statistical comparison of InSAR tropospheric correction techniques. *Remote Sens. Environ.* 170, 40–47. <https://doi.org/10.1016/j.rse.2015.08.035>
- Bell, J.W., Amelung, F., Ferretti, A., Bianchi, M., Novali, F., 2008. Permanent scatterer InSAR reveals seasonal and long-term aquifer-system response to groundwater pumping and artificial recharge. *Water Resour. Res.* 44, n/a-n/a. <https://doi.org/10.1029/2007WR006152>

- Benoit, A., Pinel-Puysségur, B., Jolivet, R., Lasserre, C., 2020. CorPhU: An algorithm based on phase closure for the correction of unwrapping errors in SAR interferometry. *Geophys. J. Int.* 221, 1959–1970.
- Bierkens, M.F., Wada, Y., 2019. Non-renewable groundwater use and groundwater depletion: a review. *Environ. Res. Lett.* 14, 063002.
- Bürgi, P.M., Lohman, R.B., 2021. High-Resolution Soil Moisture Evolution in Hyper-Arid Regions: A Comparison of InSAR, SAR, Microwave, Optical, and Data Assimilation Systems in the Southern Arabian Peninsula. *J. Geophys. Res. Earth Surf.* 126, e2021JF006158.
- Chaussard, E., Milillo, P., Bürgmann, R., Perissin, D., Fielding, E.J., Baker, B., 2017. Remote sensing of ground deformation for monitoring groundwater management practices: application to the Santa Clara Valley during the 2012–2015 California drought. *J. Geophys. Res. Solid Earth* 122, 8566–8582.
- Chen, C.W., Zebker, H.A., 2002. Phase unwrapping for large SAR interferograms: Statistical segmentation and generalized network models. *IEEE Trans. Geosci. Remote Sens.* 1709–1719.
- Cigna, F., Tapete, D., 2021. Satellite InSAR survey of structurally-controlled land subsidence due to groundwater exploitation in the Aguascalientes Valley, Mexico. *Remote Sens. Environ.* 254, 112254.
- Coleman, T.F., Li, Y., 1996. An interior trust region approach for nonlinear minimization subject to bounds. *SIAM J. Optim.* 6, 418–445.
- Colliander, A., Jackson, T.J., Bindlish, R., Chan, S., Das, N., Kim, S.B., Cosh, M.H., Dunbar, R.S., Dang, L., Pashaian, L., 2017. Validation of SMAP surface soil moisture products with core validation sites. *Remote Sens. Environ.* 191, 215–231.
- Das, N.N., Entekhabi, D., Njoku, E.G., 2010. An algorithm for merging SMAP radiometer and radar data for high-resolution soil-moisture retrieval. *IEEE Trans. Geosci. Remote Sens.* 49, 1504–1512.
- De Zan, F., Gomba, G., 2018. Vegetation and soil moisture inversion from SAR closure phases: First experiments and results. *Remote Sens. Environ.* 217, 562–572.
- De Zan, F., Parizzi, A., Prats-Iraola, P., López-Dekker, P., 2014. A SAR Interferometric Model for Soil Moisture. *IEEE Trans. Geosci. Remote Sens.* 52, 418–425. <https://doi.org/10.1109/TGRS.2013.2241069>
- De Zan, F., Zonno, M., Lopez-Dekker, P., 2015. Phase inconsistencies and multiple scattering in SAR interferometry. *IEEE Trans. Geosci. Remote Sens.* 53, 6608–6616.
- Draper, C.S., Reichle, R.H., De Lannoy, G.J.M., Liu, Q., 2012. Assimilation of passive and active microwave soil moisture retrievals. *Geophys. Res. Lett.* 39.
- Dubois, P.C., van Zyl, J., Engman, T., 1995. Measuring soil moisture with imaging radars. *IEEE Trans. Geosci. Remote Sens.* 33, 915–926. <https://doi.org/10.1109/36.406677>
- Elliott, J.R., Biggs, J., Parsons, B., Wright, T.J., 2008. InSAR slip rate determination on the Altyn Tagh Fault, northern Tibet, in the presence of topographically correlated atmospheric delays. *Geophys. Res. Lett.* 35.
- Emardson, T.R., Simons, M., Webb, F.H., 2003. Neutral atmospheric delay in interferometric synthetic aperture radar applications: Statistical description and mitigation. *J. Geophys. Res.* 108, 2231. <https://doi.org/10.1029/2002JB001781>
- Entekhabi, D., Njoku, E.G., O'Neill, P.E., Kellogg, K.H., Crow, W.T., Edelstein, W.N., Entin, J.K., Goodman, S.D., Jackson, T.J., Johnson, J., 2010. The soil moisture active passive (SMAP) mission. *Proc. IEEE* 98, 704–716.
- Farr, T.G., Jones, C.E., Liu, Z., 2016. Progress Report: Subsidence in California, March 2015–

- September 2016 (California Department of Water Resources).
- Farr, T.G., Rosen, P.A., Caro, E., Crippen, R., Duren, R., Hensley, S., Kobrick, M., Paller, M., Rodriguez, E., Roth, L., Seal, D., Shaffer, S., Shimada, J., Umland, J., Werner, M., Oskin, M., Burbank, D., Alsdorf, D., 2007. The Shuttle Radar Topography Mission. *Rev. Geophys.* 45. <https://doi.org/10.1029/2005RG000183>
- Fattahi, H., Agram, P., Simons, M., 2017. A network-based enhanced spectral diversity approach for TOPS time-series analysis. *IEEE Trans. Geosci. Remote Sens.* 55, 777–786.
- Gabriel, A.K., Goldstein, R.M., Zebker, H.A., 1989. Mapping small elevation changes over large areas: Differential radar interferometry. *J. Geophys. Res. Solid Earth* 94, 9183–9191. <https://doi.org/10.1029/JB094iB07p09183>
- Gleeson, T., Cuthbert, M., Ferguson, G., Perrone, D., 2020. Global groundwater sustainability, resources and systems in the Anthropocene. *Annu. Rev. Earth Planet. Sci.* 48, 431–463.
- Gleeson, T., Wada, Y., Bierkens, M.F., van Beek, L.P., 2012. Water balance of global aquifers revealed by groundwater footprint. *Nature* 488, 197–200.
- Goldstein, R., 1995. Atmospheric limitations to repeat-track radar interferometry. *Geophys. Res. Lett.* 22, 2517–2520.
- Green, T.R., Taniguchi, M., Kooi, H., Gurdak, J.J., Allen, D.M., Hiscock, K.M., Treidel, H., Aureli, A., 2011. Beneath the surface of global change: Impacts of climate change on groundwater. *J. Hydrol.* 405, 532–560. <https://doi.org/10.1016/j.jhydrol.2011.05.002>
- Gruber, A., Su, C.-H., Zwieback, S., Crow, W., Dorigo, W., Wagner, W., 2016. Recent advances in (soil moisture) triple collocation analysis. *Int. J. Appl. Earth Obs. Geoinformation* 45, 200–211.
- Hanssen, R.F., 2001. *Radar Interferometry: Data Interpretation and Error Analysis*. Springer.
- Jackson, T.J., Cosh, M.H., Bindlish, R., Starks, P.J., Bosch, D.D., Seyfried, M., Goodrich, D.C., Moran, M.S., Du, J., 2010. Validation of advanced microwave scanning radiometer soil moisture products. *IEEE Trans. Geosci. Remote Sens.* 48, 4256–4272.
- Jiang, J., Lohman, R.B., 2021. Coherence-guided InSAR deformation analysis in the presence of ongoing land surface changes in the Imperial Valley, California. *Remote Sens. Environ.* 253, 112160.
- Lange, M., Zühlke, D., Holz, O., Villmann, T., Mittweida, S.-G., 2014. Applications of lp-Norms and their Smooth Approximations for Gradient Based Learning Vector Quantization., in: *ESANN*.
- Lundgren, P., Casu, F., Manzo, M., Pepe, A., Berardino, P., Sansosti, E., Lanari, R., 2004. Gravity and magma induced spreading of Mount Etna volcano revealed by satellite radar interferometry. *Geophys. Res. Lett.* 31, L04602. <https://doi.org/10.1029/2003GL018736>
- Lyons, S.N., Bock, Y., Sandwell, D.T., 2002. Creep along the Imperial Fault, southern California, from GPS measurements. *J. Geophys. Res. Solid Earth* 107, ETG 12-1-ETG 12-13. <https://doi.org/10.1029/2001JB000763>
- Maghsoudi, Y., Hooper, A.J., Wright, T.J., Lazecky, M., Ansari, H., 2022. Characterizing and correcting phase biases in short-term, multilooked interferograms. *Remote Sens. Environ.* 275, 113022. <https://doi.org/10.1016/j.rse.2022.113022>
- Massonnet, D., Rossi, M., Carmona, C., Adragna, F., Peltzer, G., Feigl, K., Rabaute, T., 1993. The displacement field of the Landers earthquake mapped by radar interferometry. *Nature* 364, 138–142. <https://doi.org/10.1038/364138a0>
- Michaelides, R.J., Zebker, H.A., 2019. A Partially-Correlated SAR Interferometric Model: Addressing Closure Phase Ambiguities and Variable Soil Moisture States, in: *AGU Fall Meeting Abstracts*. pp. G21A-06.

- Mladenova, I.E., Jackson, T.J., Njoku, E., Bindlish, R., Chan, S., Cosh, M.H., Holmes, T.R.H., de Jeu, R.A.M., Jones, L., Kimball, J., Paloscia, S., Santi, E., 2014. Remote monitoring of soil moisture using passive microwave-based techniques — Theoretical basis and overview of selected algorithms for AMSR-E. *Remote Sens. Environ.* 144, 197–213. <https://doi.org/10.1016/j.rse.2014.01.013>
- Molan, Y., Lu, Z., 2020. Can InSAR coherence and closure phase be used to estimate soil moisture changes? *Remote Sens.* 12, 1511.
- Molan, Y.E., Lu, Z., Kim, J.-W., 2020. Influence of the statistical properties of phase and intensity on closure phase. *IEEE Trans. Geosci. Remote Sens.* 58, 7346–7354.
- Murray, K.D., Lohman, R.B., 2018. Short-lived pause in Central California subsidence after heavy winter precipitation of 2017. *Sci. Adv.* 4, eaar8144. <https://doi.org/10.1126/sciadv.aar8144>
- Murray, K.D., Lohman, R.B., Kim, J., Holt, W.E., 2021. An Alternative Approach for Constraining 3D-Displacements With InSAR, Applied to a Fault-Bounded Groundwater Entrainment Field in California. *J. Geophys. Res. Solid Earth* 126, e2020JB021137. <https://doi.org/10.1029/2020JB021137>
- Neely, W.R., Borsa, A.A., Burney, J.A., Levy, M.C., Silverii, F., Sneed, M., 2021. Characterization of groundwater recharge and flow in California's San Joaquin Valley from InSAR-observed surface deformation. *Water Resour. Res.* 57, e2020WR028451.
- Nolan, M., Fatland, D.R., 2003. Penetration depth as a DInSAR observable and proxy for soil moisture. *IEEE Trans. Geosci. Remote Sens.* 41, 532–537. <https://doi.org/10.1109/TGRS.2003.809931>
- Nolan, M., Fatland, D.R., Hinzman, L., 2003. DInSAR measurement of soil moisture. *IEEE Trans. Geosci. Remote Sens.* 41, 2802–2813. <https://doi.org/10.1109/TGRS.2003.817211>
- Rabus, B., Wehn, H., Nolan, M., 2010. The Importance of Soil Moisture and Soil Structure for InSAR Phase and Backscatter, as Determined by FDTD Modeling. *IEEE Trans. Geosci. Remote Sens.* 48, 2421–2429. <https://doi.org/10.1109/TGRS.2009.2039353>
- Rosen, P.A., Gurrola, E., Sacco, G.F., Zebker, H., 2012. The InSAR scientific computing environment, in: *EUSAR 2012; 9th European Conference on Synthetic Aperture Radar*. Presented at the EUSAR 2012; 9th European Conference on Synthetic Aperture Radar, pp. 730–733.
- Rosen, P.A., Hensley, S., Joughin, I.R., Li, F.K., Madsen, S.N., Rodriguez, E., Goldstein, R.M., 2000. Synthetic Aperture Radar Interferometry. *Proc IEEE* 88, 333–382.
- Rosen, P.A., Kim, Y., Kumar, R., Misra, T., Bhan, R., Sagi, V.R., 2017. Global persistent SAR sampling with the NASA-ISRO SAR (NISAR) mission, in: *2017 IEEE Radar Conference (RadarConf)*. IEEE, pp. 0410–0414.
- Torres, R., Snoeij, P., Geudtner, D., Bibby, D., Davidson, M., Attema, E., Potin, P., Rommen, B., Floury, N., Brown, M., 2012. GMES Sentinel-1 mission. *Remote Sens. Environ.* 120, 9–24.
- Ulaby, F.T., Dubois, P.C., van Zyl, J., 1996. Radar mapping of surface soil moisture. *J. Hydrol.* 184, 57–84. [https://doi.org/10.1016/0022-1694\(95\)02968-0](https://doi.org/10.1016/0022-1694(95)02968-0)
- Ulaby, F.T.M., 1981. *Microwave remote sensing: Active and passive. Volume 1 - Microwave remote sensing fundamentals and radiometry.*
- Wetzler, N., Shalev, E., Göbel, T., Amelung, F., Kurzon, I., Lyakhovskiy, V., Brodsky, E.E., 2019. Earthquake Swarms Triggered by Groundwater Extraction Near the Dead Sea Fault. *Geophys. Res. Lett.* 46, 8056–8063. <https://doi.org/10.1029/2019GL083491>
- Woodhouse, I.H., 2017. *Introduction to microwave remote sensing.* CRC press.

- Zebker, H.A., Villasenor, J., 1992. Decorrelation in interferometric radar echoes. *IEEE Trans. Geosci. Remote Sens.* 30, 950–959. <https://doi.org/10.1109/36.175330>
- Zheng, Y., Fattahi, H., Agram, P., Simons, M., Rosen, P., 2022. On Closure Phase and Systematic Bias in Multilooked SAR Interferometry. *IEEE Trans. Geosci. Remote Sens.* 60, 1–11.
- Zwieback, S., Hensley, S., Hajnsek, I., 2017. Soil Moisture Estimation Using Differential Radar Interferometry: Toward Separating Soil Moisture and Displacements. *IEEE Trans. Geosci. Remote Sens.* 55, 5069–5083. <https://doi.org/10.1109/TGRS.2017.2702099>
- Zwieback, S., Liu, X., Antonova, S., Heim, B., Bartsch, A., Boike, J., Hajnsek, I., 2016. A statistical test of phase closure to detect influences on DInSAR deformation estimates besides displacements and decorrelation noise: Two case studies in high-latitude regions. *IEEE Trans. Geosci. Remote Sens.* 54, 5588–5601.